Research Square

Preprints are preliminary reports that have not undergone peer review.
They should not be considered conclusive, used to inform clinical practice,
or referenced by the media as validated information.

# Integrated Experimental–Computational Approach to Glucose-Stabilized $Fe_3O_4$@Ag Nanocomposites: Green Synthesis, Electronic Structure, and Applications

**Niloufar abdirad**
Basque Center for Materials, Applications and Nanostructures
**sara seyfi**
University of Science and Technology of Mazandaran
**arash kamran-pirzaman**
a.kamran@mazust.ac.ir

University of Science and Technology of Mazandaran

**Research Article**

**Keywords:** DFT, HOMO–LUMO gap, interfacial charge transfer (ICT), metal-to-metal charge transfer (MMCT), Natural Bond Orbital (NBO) analysis, reduced density gradient (RDG)

**Posted Date:** July 3rd, 2026

**DOI:** https://doi.org/10.21203/rs.3.rs-9614708/v1

**License:** This work is licensed under a Creative Commons Attribution 4.0 International License.
Read Full License

**Additional Declarations:** No competing interests reported.

# Integrated Experimental–Computational Approach to Glucose-Stabilized $Fe_3O_4$@Ag Nanocomposites: Green Synthesis, Electronic Structure, and Applications

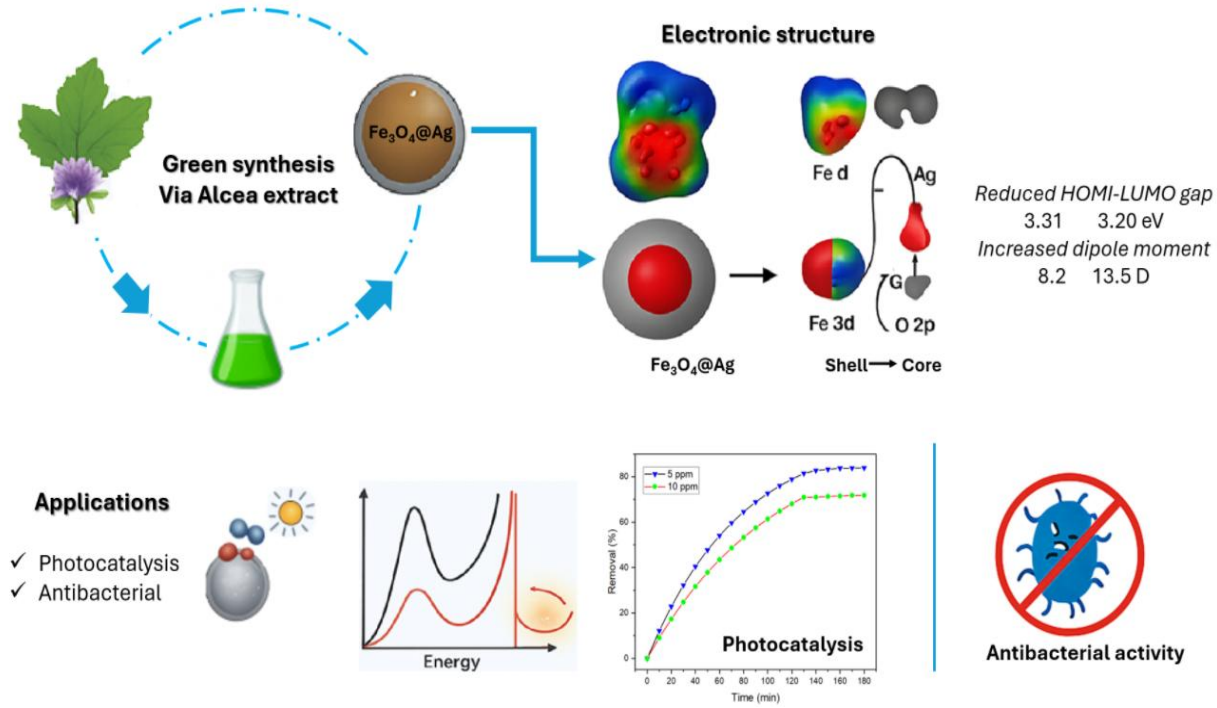
Niloufar Abdirad [a], Sara Seyfi *[b], Arash Kamran-Pirzaman [b]*

[a]BCMaterials, Basque Center for Materials, Applications and Nanostructures, UPV/EHU Science Park, 48940 Leioa, Spain

[b]Faculty of Chemical Engineering, University of Science & Technology of Mazandaran, Behshahr, Iran

*** Corresponding Author**: a.kamran@mazust.ac.ir, s.seifi@mazust.ac.ir

## Graphic abstract



**Abstract**: Magnetic silver core–shell nanoparticles ($Fe_3O_4$@Ag) were synthesized via a sustainable green chemistry route using Alcea leaf extract, which acted as both reducing and stabilizing agent. Optimization of the extract concentration yielded uniform nanostructures with a silver coating efficiency of 88.7%, an average size of 95.4 nm, and good colloidal stability (zeta potential −27.2 mV). Structural characterization (EDX, XRD, FT-IR, SEM) confirmed the formation of the desired core–shell morphology.

To rationalize the experimental observations, density functional theory (DFT) and time-dependent DFT (TDDFT) calculations were performed on a glucose-stabilized $Fe_3O_4$@Ag cluster. Theoretical analyses revealed orbital hybridization between Fe 3d, O 2p, and Ag states, with glucose introducing new Ag–O(C) contributions near the Fermi level. Frontier orbital analysis indicated a switch in the charge-transfer pathway, from interfacial core→shell transfer in the pristine system to shell→core metal-to-metal transfer after glucose adsorption. This orbital realignment reduced the HOMO–LUMO gap (3.31 → 3.20 eV) and increased the dipole moment (8.2 → 13.5 D), consistent with the experimentally observed zeta potential and red-shift in UV–Vis absorption. Non-covalent interaction analyses showed that stabilization is driven by physisorption through van der Waals and weak hydrogen-bond–like electrostatic contacts (O···Ag 2.4–2.7 Å, O–H···Ag 1.9–2.2 Å, ∠ ~92–107°), rather than covalent bonding.

**Keywords**: DFT; HOMO–LUMO gap; interfacial charge transfer (ICT); metal-to-metal charge transfer (MMCT); Natural Bond Orbital (NBO) analysis; reduced density gradient (RDG).

## 1. Introduction

Nanotechnology has emerged as a transformative field with wide-ranging applications in catalysis [1], biomedicine [2], and environmental remediation [3]. Green synthesis strategies have gained

particular attention [4] because they minimize ecological risks compared to conventional methods that often rely on toxic reagents [5] and high energy input [6]. Among various biological approaches, plant extracts are especially attractive due to their rich biomolecular contents such as flavonoids [7], polyphenols [8], and carbohydrates [9] that simultaneously act as reducing [10], capping, and stabilizing agents [11].

Metal and metal–oxide nanostructures have been extensively studied for their tunable optical [12], magnetic [13], and antimicrobial properties [14]. Core–shell architectures are of particular interest because they integrate distinct functionalities [15] while reducing material costs by using inexpensive cores coated with noble metals [16–19]. Within this class, $Fe_3O_4$@Ag hybrid nanostructures have emerged as promising multifunctional platforms: $Fe_3O_4$ provides biocompatibility [20] and magnetic responsiveness [21], whereas Ag contributes strong plasmonic [22] and antimicrobial properties [23–26]. Green synthetic routes for Ag [27] and $Fe_3O_4$ nanoparticles [28] using plant-derived molecules such as glucose [29,30] have been reported, highlighting their role in enhancing colloidal stability and bifunctionality.

Several recent works illustrate these advances: Ahmed et al. demonstrated the facile plant-mediated synthesis of Ag nanoparticles with enhanced antimicrobial activity [31]; Sarkar and Mandal reported glucose-assisted fabrication of size-controlled $Fe_3O_4$ nanocrystals [32]; Rukhsar et al. provided a comprehensive review of the structural and magnetic properties of $Fe_3O_4$ nanoparticles for biomedical applications [33]; and Abdel-Hafez et al. highlighted the broad-spectrum antimicrobial properties of Ag-based nanostructures [34].

Despite significant experimental progress, the molecular-level mechanisms underlying nanoparticle stabilization by plant-derived biomolecules remain poorly understood. In particular, the role of glucose in modulating the electronic structure and charge-transfer pathways of

$Fe_3O_4$@Ag systems has not been elucidated. Previous studies have demonstrated catalytic [35] and biosensing applications [36] of $Fe_3O_4$@Ag nanoparticles, and glucose has been used as a capping agent for $Fe_3O_4$ [37] and Ag nanoparticles [38,39]. However, no theoretical (DFT/TDDFT) work has yet addressed the $Fe_3O_4$@Ag–glucose interface, orbital reorganization, or interfacial charge-transfer mechanisms.

Numerous experimental studies have demonstrated the green synthesis of $Fe_3O_4$@Ag nanocomposites. However, the molecular mechanisms underlying their surface stabilization by plant-derived carbohydrates remain poorly understood. In particular, the specific surface sites responsible for glucose adsorption are not yet clearly identified, and it is unclear whether these interactions are governed primarily by electrostatic forces or involve orbital-level charge transfer. Understanding these processes is essential for establishing reliable structure–property relationships in hybrid nanomaterials produced via green synthesis.

The present study combines green synthesis and multiscale characterization with first-principles calculations to bridge this gap. We demonstrate that glucose adsorption drives a switch from interfacial charge transfer (ICT, core→shell) in pristine $Fe_3O_4$@Ag to a metal-to-metal charge transfer (MMCT, shell→core) configuration. This ICT→MMCT transition is quantified through orbital decomposition and correlated with experimental UV–Vis red-shifts and dipole enhancements, providing fundamental insights for the rational design of stable, multifunctional nanostructures.

## 2. Experimental

### 2.1. Materials and physical methods

Iron (III) chloride hexahydrate ($FeCl_3 \cdot 6H_2O$, 99 wt%, CAS No. 10025-77-1), silver nitrate ($AgNO_3$, 99.9 wt%, CAS No. 7761-88-8), iron (II) chloride tetrahydrate ($FeCl_2 \cdot 4H_2O$, 99 wt%, CAS No. 13478-10-9), and sodium hydroxide (NaOH, 98 wt%, CAS No. 1310-73-2) were obtained from Merck Co., Germany. The morphology and size distribution of the nanoparticles were investigated using a Field Emission Scanning Electron Microscope (FE-SEM, JEOL JSM-7610F). The elemental composition and silver coating efficiency were analyzed by Energy Dispersive X-ray Spectroscopy (EDX, Oxford Instruments X-MaxN 80), confirming the presence of Fe, O, and Ag with a coating efficiency of 88.65%. The crystallinity and phase structure were determined by X-ray Diffraction (XRD, PANalytical X'Pert PRO, Cu Kα radiation, $\lambda = 1.5406$ Å). Fourier-transform infrared spectra (4000–400 $cm^{-1}$) of powdered samples were obtained as KBr pellets using a PerkinElmer Spectrum Two FT-IR spectrometer. UV–Vis absorption spectra were recorded on a UV–Vis spectrophotometer (HACH DR 6000) using a quartz cuvette of 1 cm path length at room temperature. Thermal stability was assessed by Thermogravimetric Analysis (TGA, TA Instruments Q50) under nitrogen atmosphere at a heating rate of 10 °C/min.

### 2.2.Experimental Methods

The $Fe_3O_4$ core and $Fe_3O_4$@Ag core–shell nanoparticles were synthesized through a two-step green chemistry route using Alcea leaf extract as a natural reducing and stabilizing agent. All reagents were of analytical grade and used as received. Plant material was collected from the Faculty of Agriculture, Razi University. A complete list of chemicals, their purity, instrumentation specifications, and the full synthesis protocols are provided in the Supporting Information.

#### 2.2.1. Synthesis of $Fe_3O_4$ Nanoparticles

$Fe_3O_4$ nanoparticles were prepared by a coprecipitation method. Aqueous solutions of Fe (II) and Fe (III) chloride salts were mixed, followed by the addition of Alcea extract. The pH was adjusted to 11 using sodium hydroxide, which initiated precipitation. The resulting nanoparticles were magnetically separated, washed with distilled water, and dried. Detailed concentrations and procedural parameters are available in Supporting Information.

### 2.2.2. Synthesis of $Fe_3O_4$@Ag Core–Shell Nanoparticles

$Fe_3O_4$@Ag nanostructures were synthesized via a one-pot green route. Pre-synthesized $Fe_3O_4$ nanoparticles were combined with silver nitrate and Alcea extract under controlled heating, where plant biomolecules facilitated the reduction of $Ag^+$ ions and deposition of a silver shell. Process optimization was performed using a Central Composite Design (CCD) within Design-Expert software (version 13). Final products were magnetically collected, washed, and dried. The complete optimization matrix is given in the Supporting Information.

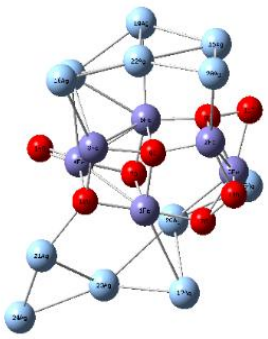
## 3. Computational Methods

All quantum-chemical calculations were performed with the Gaussian 16 package [40]. Geometry optimizations were carried out using the CAM-B3LYP functional in conjunction with the LANL2DZ effective core potentials (ECPs) for Fe and Ag atoms [41] and the 6-311G(d) basis set for C, H, and O atoms [42]. The CAM-B3LYP functional was chosen because long-range corrected hybrids reliably describe charge-transfer excitations in metal/oxide–organic systems, where conventional hybrids such as B3LYP often underestimate excitation energies [43]. The polarizable continuum model (PCM) with water as solvent was employed to account for solvation effects consistently in both ground and excited states [44].

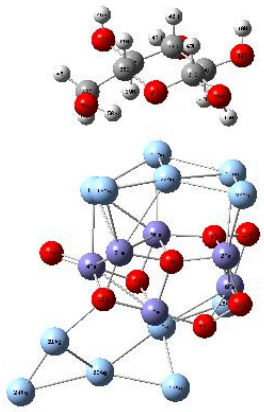
The modeled systems included (i) a cluster fragment of the $Fe_3O_4$ (111) surface to represent the magnetite core, (ii) a monolayer Ag shell forming the core–shell structure, (iii) an isolated glucose molecule, and (iv) the $Fe_3O_4$@Ag–glucose complex **(Fig.1a, b)**. Core Fe–O atoms were kept frozen to preserve local crystallographic integrity, while the Ag shell and glucose molecule were fully relaxed during optimization. The cluster was constructed by trimming a full $Fe_3O_4$ unit cell, as shown in the Supporting Information (**Fig. S1-3**), ensuring that the essential local coordination and interfacial chemistry were maintained.

Time-dependent DFT (TDDFT) calculations at the same CAM-B3LYP/LANL2DZ/6-311G(d) level were performed to obtain excitation energies and oscillator strengths, which were further analyzed with GaussSum [45]. Natural Bond Orbital (NBO) analysis was used to quantify donor–acceptor interactions [46]. Density of states (DOS) and projected DOS (PDOS) were generated with Multiwfn 3.3.9 [47], and frontier molecular orbitals were visualized using GaussView 6.0 [48]. Reduced density gradient (RDG) analysis was also employed to probe non-covalent interactions at the $Fe_3O_4$@Ag–glucose interface [49].

The cluster approach adopted here has been widely used for $Fe_3O_4$@Ag and other metal–oxide@Ag systems, capturing essential charge-transfer physics in agreement with experimental data [50,51]. While periodic DFT would provide further validation, the present finite model is sufficient to interpret the experimental optical and electronic trends addressed in this work.



(a)



(b)

**Fig. 1.** (a) Optimized structure of the $Fe_3O_4$@Ag core–shell system, showing the magnetite core encapsulated by a silver shell. (b) Optimized structure of glucose adsorbed on the $Fe_3O_4$@Ag core–shell surface. The glucose molecule interacts primarily with the Ag shell, demonstrating the adsorption configuration studied.

In this study, a cluster model was constructed to capture the essential local coordination features of the $Fe_3O_4$@Ag interface, rather than to reproduce the full nanoparticle geometry. Previous theoretical investigations have demonstrated that finite cluster models can effectively describe key interfacial phenomena in metal/metal-oxide hybrid systems, such as charge-transfer behavior, adsorption energetics, and orbital reorganization. To minimize artificial edge effects, the inner Fe–O framework was kept fixed, while the surface Ag atoms and adsorbed species were allowed to relax fully. This approach provides a practical balance between physical accuracy and computational cost.

## 4. Results and Discussion

### 4.1.Geometry Optimization and Interfacial Interaction

The strength of the interaction between glucose and the $Fe_3O_4$@Ag surface was evaluated by calculating the adsorption energy (E_ads), defined as:

$$E_{\text{ads}} = E_{\text{complex}} - (E_{\text{surface}} + E_{\text{glucose}})$$

Here, $E_{\text{complex}}$represents the total energy of the optimized glucose–$Fe_3O_4$@Ag system, while $E_{\text{surface}}$and $E_{\text{glucose}}$correspond to the energies of the isolated $Fe_3O_4$@Ag cluster and the free glucose molecule, respectively. A negative E_ads value indicates that adsorption is energetically favorable. The calculated adsorption energy shows that glucose preferentially binds to the Ag shell,

consistent with its experimentally observed role as a stabilizing and capping agent during nanoparticle formation.

preservation of the spherical core–shell framework. The absence of imaginary vibrational frequencies validated that the system had converted to a real minimum energy structure. Upon adsorption of glucose, weak hydrogen bond was formed between surface silver atoms and the hydroxyl (–OH) group of glucose was formed, with H···Ag and O···Ag distances of approximately 2.40 Å **(Fig. 2)** [52,53]. Even though this is non-covalent interaction, it significantly stabilizes nanoparticles in aqueous media through glucose attachment to the Ag surface [54]. The optimized O–H···Ag contacts are 1.94–2.16 Å with O–H···Ag angles of ~92–107°, consistent with weak hydrogen bonding or electrostatic stabilization rather than strong directional hydrogen bonding. Additional O(glucose)···Ag contacts occur at 2.4–2.7 Å (see SI, **Table S1**). In our work, glucose acted as both a mild reducing agent—capable of reducing $Ag^+$ ions in situ—and an adsorbing capping molecule for stabilizing nanoparticles [55,56]. These functions are inherently interconnected, with glucose adsorption being a direct consequence of nanoparticle stability and formation. Theoretical calculation is also shown to reveal that glucose not only participates in the synthesis of the nanoparticle but also regulates the electronic environment of the Ag shell by weak physisorption and orbital interactions [57]. This control enhances colloidal stability and visible-light activity. Besides, glucose adsorption plays a role in modifying frontier molecular orbital distribution, promoting charge separation and improving light-harvesting efficiency in the visible region [58,59].

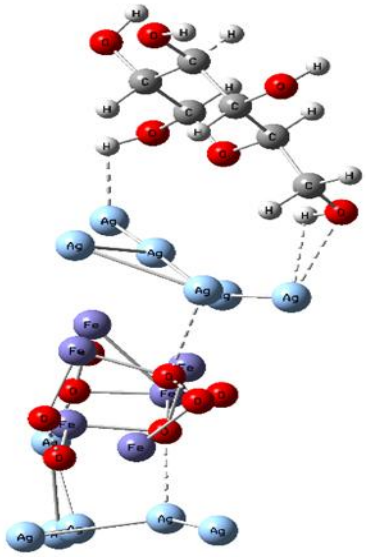


**Fig. 2.** Optimized geometry of glucose adsorbed on the $Fe_3O_4$@Ag core–shell cluster, showing O···Ag contact distances (2.4–2.7 Å) and O–H···Ag angles (~92–107°).

### 4.2. Investigation of particle size and size dispersion index of nanoparticles (Poly dispersity index- PDI)

The dispersion of nanoparticles within the dispersant and their co-accumulation are crucial factors in preparing suspensions and are directly related to the particles' surface charge. Zeta potential represents the repulsive forces between particles of the same charge in the suspension. A higher absolute value of zeta potential indicates that the particles in the suspension are less likely to agglomerate. Dynamic Light Scattering (DLS) analysis was employed to determine the size of the nanoparticles. This analysis provided the hydrodynamic radius of the nanoparticles and their Polydispersity Index (PDI), as shown in **Table 1.** Based on the data presented in the table, the sample with the smallest dynamic radius and the highest surface charge was identified as the optimal choice.

**Table 1.** The results of DLS analysis of magnetite-silver composite nanoparticles

| No. sample | $R_{hyd}$ | PDI | Zeta |
|---|---|---|---|
| 1 | 181.1 | 0.297 | -26.4 |
| 2 | 198.2 | 0.301 | -14.2 |
| 3 | 156 | 0.325 | -13.6 |
| 4 | 175.2 | 0.444 | -25.9 |
| 5 | 95.44 | 0.257 | -27.2 |
| 6 | 243.9 | 0.577 | -19.1 |
| 7 | 201.3 | 0.368 | -24.4 |
| 8 | 310 | 0.541 | -16.6 |
| 9 | 259 | 0.421 | -14.6 |

The results revealed that composite nanoparticles synthesized under varying concentration conditions exhibited different hydrodynamic radii and particle size distribution indices. Among the magnetic-silver composite nanoparticles, sample 5 demonstrated smaller particle size and a more favorable dispersion index compared to the other samples, indicating the formation of uniform, homogeneous nanoparticles (**Fig.3** and **Fig.4**). This sample was chosen for further investigation.

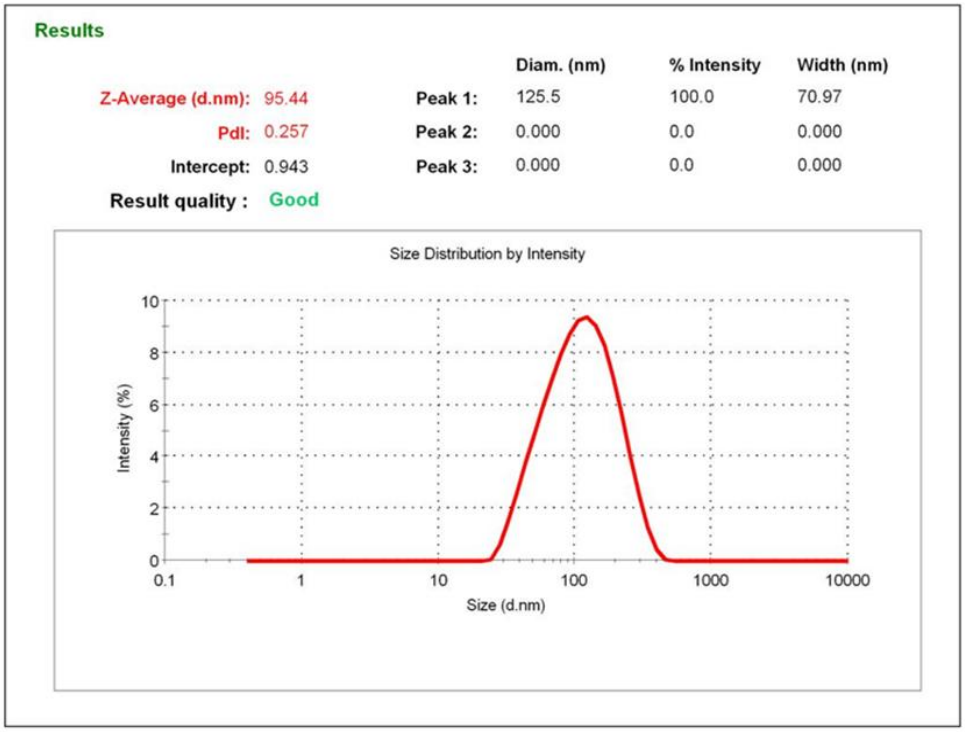



**Fig. 3.** Dynamic Light Scattering (DLS) analysis of the sample showing a single peak with a Z-average hydrodynamic diameter of 95.44 nm and a PDI of 0.257, indicating a narrow and monodisperse size distribution (quality rated as "Good," intercept = 0.943).

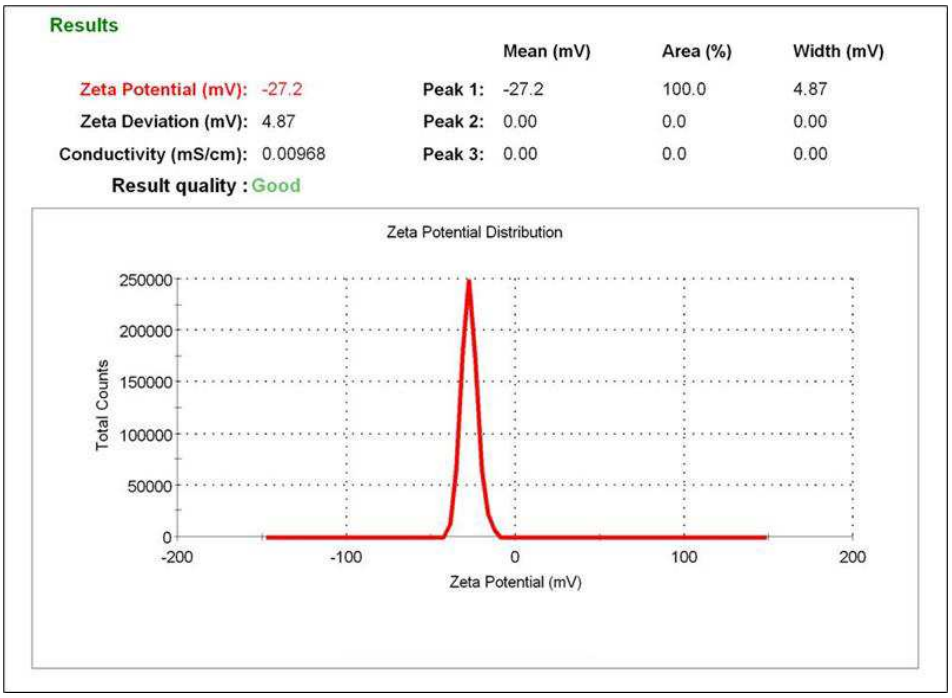


**Fig. 4.** Zeta potential distribution of the particles, showing a single peak with an average value of –27.2 mV, indicating that the particles carry a negative surface charge.

### 4.3.Investigation of the X-ray diffraction (XRD) diagram

To identify and characterize the crystal structure of composite nanoparticles synthesized via the green method, X-ray diffraction (XRD) analysis was employed. XRD is a technique used to investigate the structure of crystalline materials, allowing for the analysis of phase, crystal structure, and interplanar spacing of the nanoparticles. This process involves the examination of X-ray reflections from the sample surface [60].

The samples were prepared in a completely dry powder form, free of any moisture. By systematically varying the angle of the incident X-ray beam on the sample, a spectrum of varying intensity was recorded as a function of the angle between the incident and scattered beams. X-ray diffraction spectroscopy enabled the identification of the material type, phase characteristics, and the distances between crystal planes [61]. This analysis relied on the processing and interpretation of the X-ray reflections from the sample surface. As **Fig.5** Shows, the XRD pattern matches literature structure [62, 63].

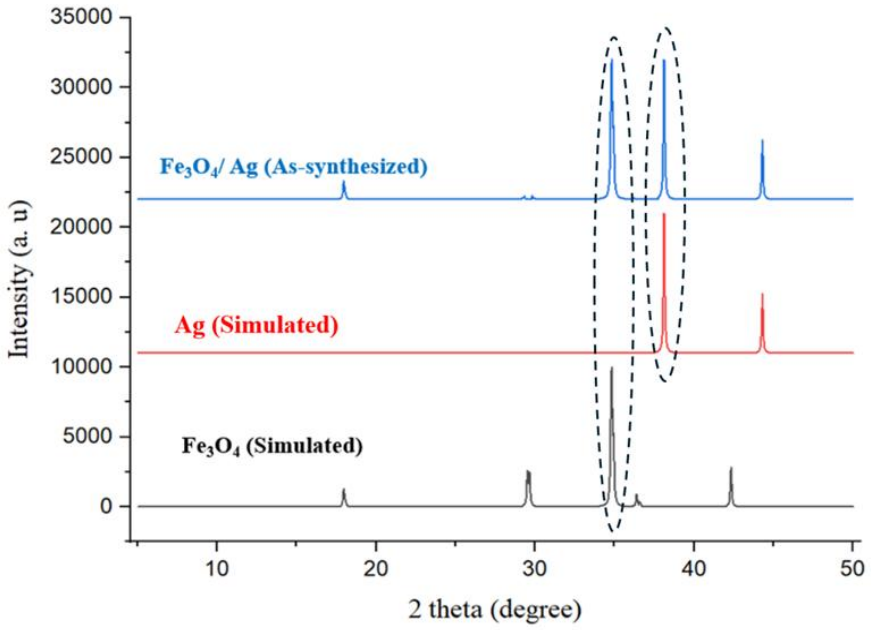



**Fig. 5.** XRD patterns show the as-synthesized $Fe_3O_4$@Ag sample together with simulated patterns of pure $Fe_3O_4$ and Ag, clearly illustrating the presence of both phases in the composite.

### 4.4.Investigation of nanoparticle morphology by Scanning Electron Microscopy (SEM)

As it showed in **Fig. 6**, according to the result obtained from the SEM image, it was found that sample number 5, which had the smallest size and the highest surface charge, has a spherical and relatively uniform morphology. Meanwhile, checking the average particle size (79.05 nm) with ImageJ software confirmed the result. Also, the synthesized particles have an acceptable uniformity.

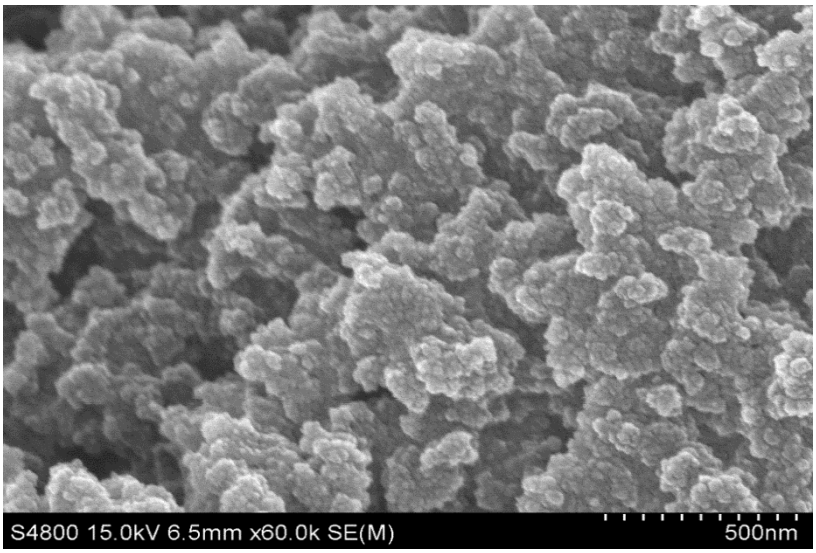



**Fig. 6**. SEM image obtained from magnetite-silver composite nanoparticles

### 4.5.Investigation of nanoparticle by Energy Dispersive X-ray (EDX*)*

Energy Dispersive X-ray (EDX) was used to check the elements in the synthesized sample and its qualitative/quantitative analysis. As we can see in **Fig.7** and **Fig. 8**, this investigation made it clear that the presence of silver (Ag) and Iron (Fe) elements in our sample. Also, elements such as carbon (c) and oxygen (o)are due to the use of plant extracts (Glucose ($C_6H_{12}O_6$)) in the sample synthesis process. So, it can be confirmed that the green synthesis of $Fe_3O_4$@Ag core-shell nanoparticles has been done correctly.

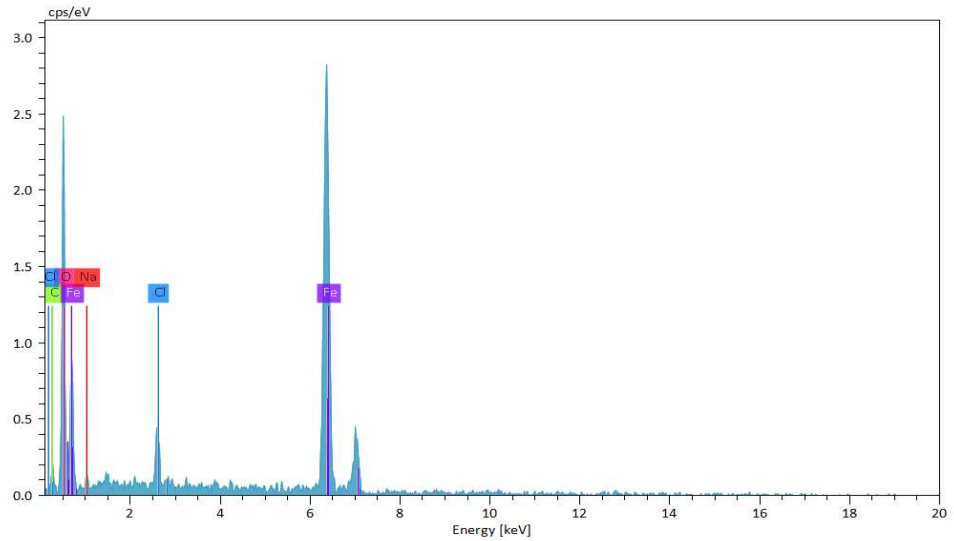



**Fig. 7.** X-ray energy dispersive spectroscopy (EDS) analysis of the iron oxide nanoparticles, confirming the presence of iron (Fe) and oxygen (O) as the primary elemental components.

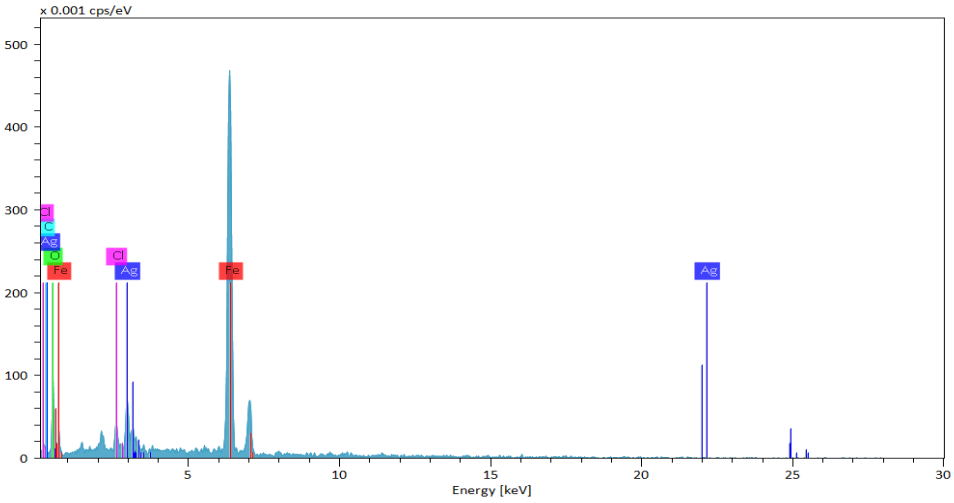



**Fig. 8.** X-ray energy dispersive spectroscopy (EDS) analysis of the magnetite-silver composite nanoparticles, confirming the presence of iron (Fe), oxygen (O), and silver (Ag) in the sample.

### 4.6.Investigation of the Thermogravimetric Analysis (TGA) Diagram

Thermogravimetric Analysis (TGA) is a technique used to measure changes in the weight of a sample as a function of temperature or time in a controlled atmosphere. This method helps determine the composition of materials and predict their thermal stability up to temperatures as high as 1500 °C [64]. As shown in **Fig. 9**, the sample loses approximately 6% of its weight by 90 °C, which is attributed to the evaporation of physisorbed water, low-molecular-weight volatile compounds, solvents, and trapped gases. Between 150 °C and 250 °C, the mass reduction is due to the loss of chemisorbed water and low-molecular-weight compounds, such as additives and volatile decomposition products. Beyond 250 °C, the sample begins to decompose, with multiple onset and endset temperatures possible for multi-component systems or reactions involving intermediate steps. By 520 °C, around 55% of the sample has decomposed or evaporated, and between 520 °C and 800 °C, the remaining 45% of the mass is residual ash from the thermal degradation process.

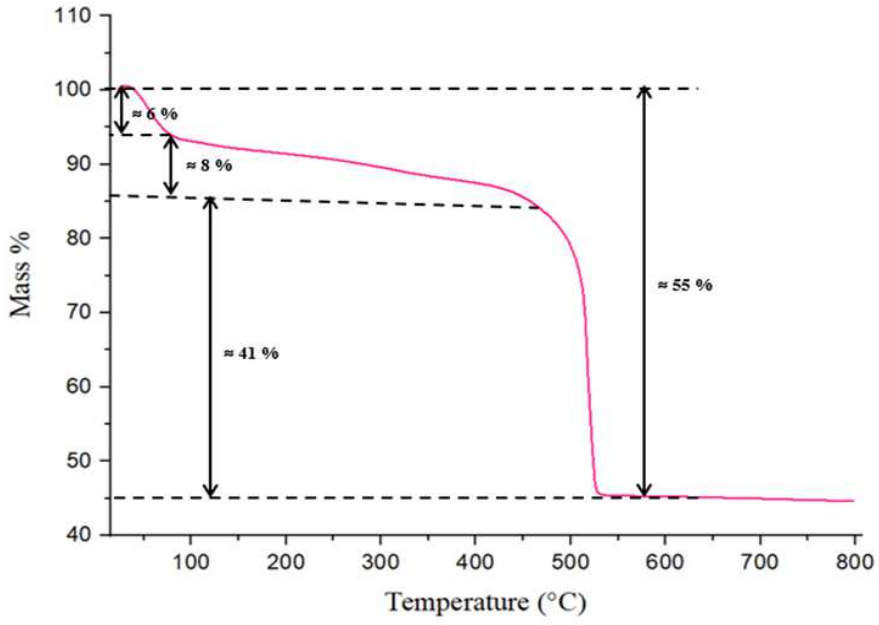


**Fig. 9.** Thermogravimetric analysis (TGA) curve showing the mass loss profile of the sample as a function of temperature, indicating successive weight reductions due to moisture release, volatile components, and major thermal degradation.

All characterization analyses of the synthesized nanoparticles, including SEM, FTIR, and EDX, are provided in full in the Supporting Information. These data comprehensively confirm the morphology, composition, and structural features of $Fe_3O_4$@Ag nanocomposites.

### 4.7.Investigation of the results of Fourier transform infrared (FT-IR)

Based on the chemical structure and FTIR spectrum of the magnetite-silver nanoparticles (**Fig. 10**), the peak observed at 3424 $cm^{-1}$ can be attributed to the hydroxyl group (OH). The peak at 2924 $cm^{-1}$ is a result of stretching vibrations between carbon and hydrogen (C-H), typically occurring within the 2800 $cm^{-1}$ to 3300 $cm^{-1}$ range. The peak near 1618 $cm^{-1}$ likely corresponds to overlapping signals from alkene (C=C) or carbonyl (C=O) groups, due to the presence of Alcea extract coating the nanoparticles. The characteristic C-O stretching vibrations, both aliphatic and aromatic, generally appear in the 1000 $cm^{-1}$ to 1350 $cm^{-1}$ range [65–67].

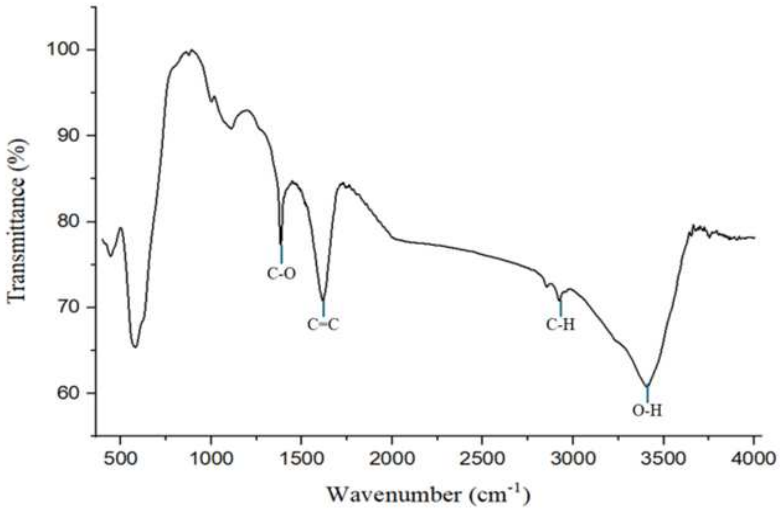


**Fig. 10.** FTIR spectrum of the magnetite-silver nanoparticles, showing the characteristic confirming the presence of organic functional groups on the nanoparticle surface.

### 4.8.Electrostatic Surface Potential and Charge Distribution

Electrostatic surface potential (ESP) mapping and Mulliken charge analysis revealed strong polarity across the $Fe_3O_4$@Ag core–shell nanostructure (**Fig. 11**). Oxygen atoms of the $Fe_3O_4$ core carry partial negative charges while the silver atoms of the shell possess weak positive character [68, 69]. This charge asymmetry results in a net dipole moment of 8.2 Debye for the core–shell nanostructure (**Fig. 12**), in qualitative agreement with the experimentally measured zeta potential of −27.2 mV [70]. Such intrinsic polarity facilitates dipole–dipole and hydrogen bonding interactions with biomolecules, fostering colloidal stability and bioactivity [71,72]. In the pristine system, HOMO is localized on the Fe–O core and LUMO on the Ag shell (core→shell ICT). Upon glucose adsorption, the HOMO shifts to the Ag shell at the glucose binding site, while the LUMO+7 is located on the $Fe_3O_4$ core/interface, consistent with shell→core MMCT. Glucose interacts with the Ag shell, modulating the electronic environment and facilitating metal-to-metal charge transfer [73,74]. This interaction enhances charge separation and overall polarity, potentially improving the nanostructure's electronic properties and its affinity for biomolecular interactions [75]. The ESP map of the $Fe_3O_4$@Ag-glucose complex (**Fig. 13**) demonstrates modified charge distribution and enhanced polarity upon glucose adsorption. Potential donor and acceptor sites of glucose, identified via ESP mapping (Fig. S3), support its electron-donating role during adsorption [76]. All ESP maps use a color scale of −0.05 a.u. (electron-rich, red) to +0.05 a.u. (electron-deficient, blue) with the molecular surface at isovalue 0.001 e/bohr$^3$.

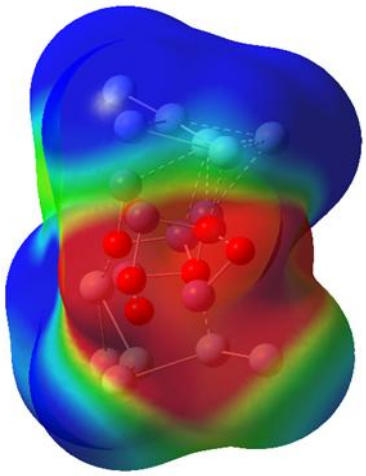


**Fig. 11.** Electrostatic surface potential (ESP) map of the $Fe_3O_4$@Ag core–shell nanostructure, showing charge distribution and polarity.

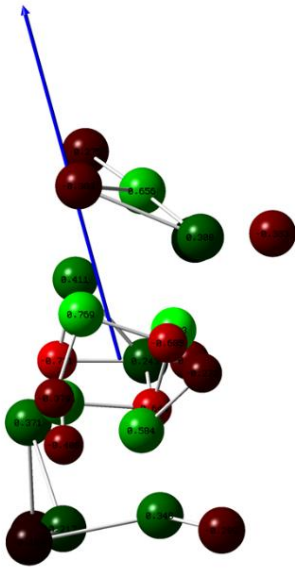


**Fig. 12**. Mulliken charges indicating negative O and slightly positive Ag atoms in the core–shell structure. The blue arrow indicates the dipole moment vector.

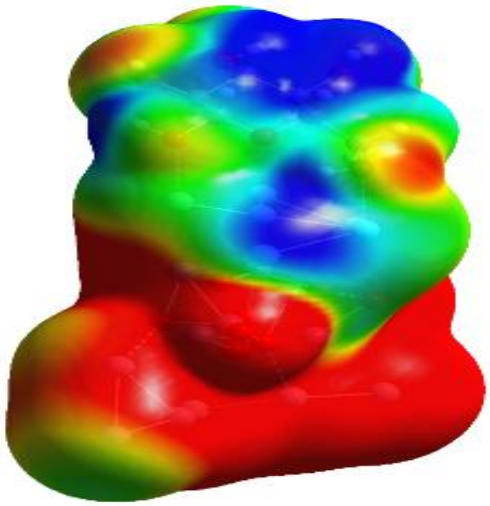


**Fig. 13.** Electrostatic surface potential (ESP) map of the $Fe_3O_4$@Ag core–shell - glucose nanostructure, showing charge distribution and polarity.

### 4.9.Frontier Orbitals and Charge Transfer Mechanism

**Fig.14** shows that TDDFT orbital analysis of the pristine $Fe_3O_4$@Ag system exhibits the HOMO localized mainly on the Fe–O core, while the LUMO and LUMO+5 are delocalized over the Ag shell. This orbital alignment favors interfacial charge transfer (ICT) from the magnetic core to the plasmonic shell upon photoexcitation [77]. Upon glucose adsorption, the dominant excited-state transition shifts to HOMO → LUMO+7. In this case, the HOMO is localized over the Ag shell near the glucose binding site, while the LUMO+7 is distributed over the $Fe_3O_4$ core and the Ag–Fe interface (**Fig.15**). This spatial separation indicates a metal-to-metal charge transfer (MMCT) from shell to core, promoting visible-light absorption and extending the lifetime of charge carriers [78,79]. Redistribution of electrons also increases the dipole moment, which favors greater electrostatic interactions with bacterial membranes or other polar analytes [80].PDOS/NBO decomposition further quantifies these contributions: in the pristine $Fe_3O_4$@Ag system the HOMO is ~65–70% Fe 3d and 25–30% O 2p, whereas LUMO/LUMO+5 are ~70–75% Ag 5s/5p with

minor Fe admixture. Upon glucose adsorption, the HOMO at the binding site contains ~55–65% Ag with ~10–20% O/C (glucose), and LUMO+7 is ~60–70% Fe 3d at the core/interface. This redistribution confirms the ICT (core→shell) → MMCT (shell→core) switch (**Table S2**). These donations form delocalization within the $Fe_3O_4$ core, Ag shell, and glucose adsorption sites, creating an ICT process controlled by glucose adsorption. The oscillator strength at high level shows that the transition is optically allowed, being responsible for the experimental and theoretical increases in visible-light absorption observed [81,82]. These findings form the mechanistic role of glucose within orbital realignment, charge redistribution, and optical enhancement. Additional HOMO to HOMO-2 and LUMO to LUMO-2 plots for glucose, pristine $Fe_3O_4$@Ag, and $Fe_3O_4$@Ag–glucose are provided in the Supporting Information (**Fig. S4–S6**) to illustrate the orbital redistribution upon adsorption.

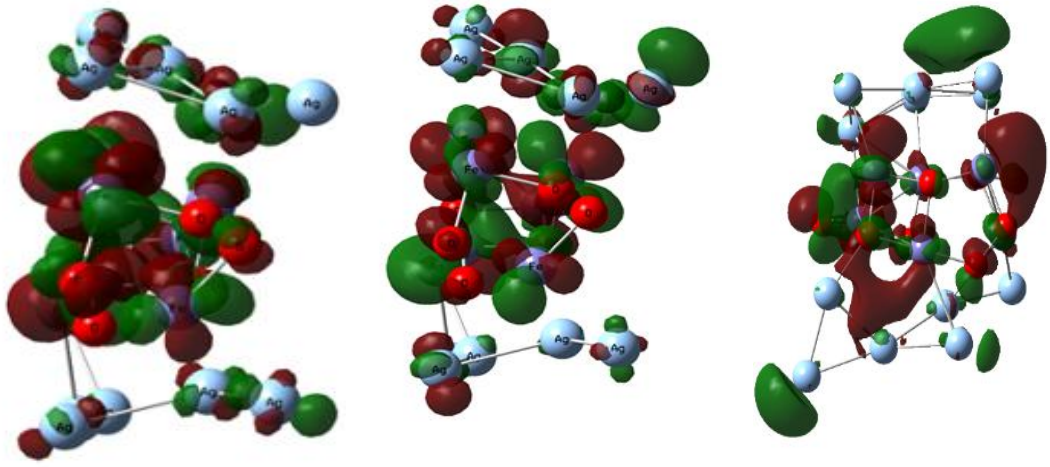
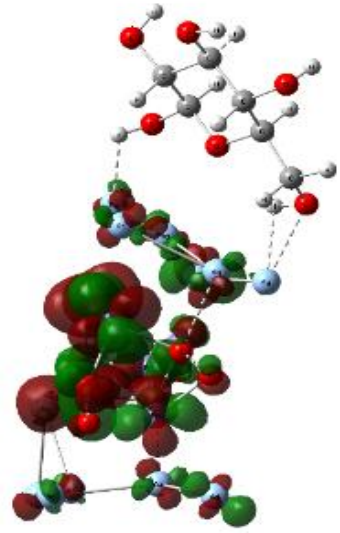
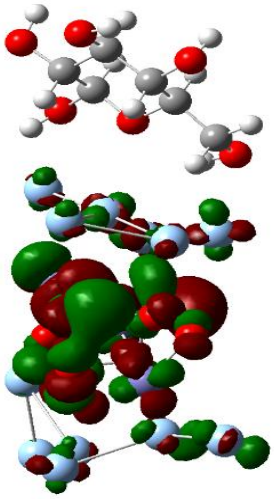


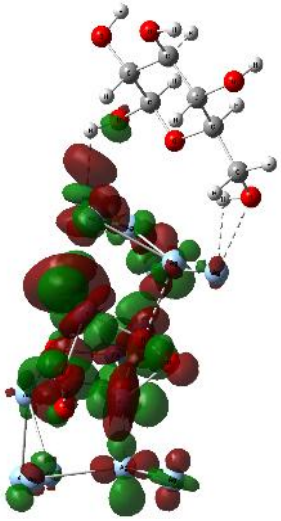

**Fig. 14.** TDDFT frontier orbitals of pristine $Fe_3O_4$@Ag: HOMO on the Fe–O core; LUMO and LUMO+5 on the Ag shell. This core→shell alignment supports interfacial charge transfer (ICT) upon photoexcitation.



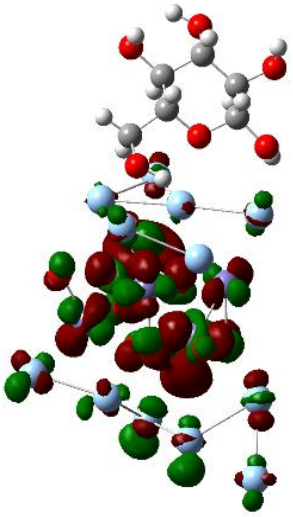
HOMO



LUMO+7



HOMO-1



LUMO+6

**Fig. 15.** Dominant excited-state channel after glucose adsorption (HOMO → LUMO+7): HOMO on the Ag shell near the glucose binding site; LUMO+7 on the $Fe_3O_4$ core@Ag–Fe interface. The spatial separation indicates MMCT (shell→core).

### 4.10. Adsorption Energy and Non-Covalent Interaction Analysis

To evaluate the interaction strength between glucose and the $Fe_3O_4$@Ag core-shell system, the adsorption energy (Eads) was calculated using the formula [83]:

(E glucose + E core shell) –E complex= Eads (1)

where, E glucose, E core shell, E complex system, the isolated core-shell, and glucose molecule, respectively. Negative Eads indicates exothermic, thermodynamically favorable adsorption. ZPE, thermal, and Gibbs corrections are reported in **Table S3**. The ZPE-corrected Eads is −158.6 kJ·mol$^{-1}$ (−1.64 eV) and the Gibbs free energy change is −89.2 kJ·mol$^{-1}$, confirming exothermic, favorable adsorption. The negative values indicate that glucose adsorption on the $Fe_3O_4$@Ag core–shell surface is thermodynamically favorable. The magnitude of these energies, combined with structural and Natural Bond Orbital (NBO) analyses, confirms that the adsorption is dominated by physisorption, involving weak hydrogen bonding and van der Waals forces, without covalent bond formation [84–86]. Non-Covalent Interaction (NCI) and NBO analyses revealed localized weak attractive contacts between hydroxyl groups of glucose and surface Ag atoms. The optimized O–H···Ag contacts are 1.94–2.16 Å with O–H···Ag angles of ~92–107°, which are too bent to qualify as classical, strong hydrogen bonds. Instead, they correspond to weak hydrogen-bond–like or electrostatic interactions, typical for physisorption on metal surfaces. Additional O···Ag contacts (2.4–2.7 Å) further support weak coordination. These individually weak interactions act cooperatively to stabilize the glucose–nanoparticle complex, enhance colloidal stability, and preserve structural integrity (**Table** S1). Correspondingly, NBO second-order perturbation energies E(2) < 2.5 kcal·mol$^{-1}$ indicated minimal charge transfer and no covalent bonding. Such individually weak interactions act cooperatively to stabilize the glucose–nanoparticle complex, enhance colloidal stability, and maintain structural integrity.

Further insight into the adsorption mechanism was gained from NBO second-order perturbation analysis. The identification of LP(O) → LP*(Ag) donor–acceptor interactions, with stabilization energies of up to approximately 11 kcal·mol$^{-1}$, indicates a non-negligible orbital overlap between the hydroxyl groups of glucose and surface Ag atoms. While these interactions are substantially weaker than typical covalent bonds, their magnitude exceeds that expected for purely electrostatic attraction. This finding supports an adsorption mechanism with mixed physisorptive and coordinative character, which can induce measurable perturbations in the surface electronic structure and is consistent with the observed HOMO–LUMO level reorganization.

Natural Population Analysis (NPA) indicated that oxygen atoms O31 and O32 in glucose carry the most negative charges (−0.72475 and −0.75881, respectively), consistent with their role in hydrogen bonding. In addition, a small n→n∗ interaction between the lone pair of O32 and antibonding LP* orbitals of Ag atoms (2.01 kcal·mol$^{-1}$) was observed, contributing to overall stability. These findings agree with previous computational and spectroscopic reports on carbohydrate adsorption on plasmonic and metal–oxide surfaces, where physisorption is complemented by hydrogen bonding and dispersion forces [87,89].

Furthermore, NBO second-order perturbation analysis reveals multiple donor–acceptor interactions within the $Fe_3O_4$@Ag core–shell–glucose complex. Notably, lone pairs on oxygen atoms donate electron density into antibonding orbitals on Ag, with stabilization energies ranging from 1.5 to 11.3 kcal·mol$^{-1}$, indicative of weak to strong coordination interactions. Additionally, significant MMCT pathways are evident, such as the Fe1–O10 bonding orbital to Ag21 antibonding orbital (3.71 kcal·mol$^{-1}$) (**Table S4**). These charge transfers facilitate effective

electronic coupling at the core–shell interface, contributing to the enhanced optoelectronic properties of the hybrid nanostructure.

NBO second-order perturbation energies E(2) for donor–acceptor interactions are ≤ 2–3 kcal·mol$^{-1}$ for LP(O_glc)→LP(Ag) contacts and 1–11 kcal·mol$^{-1}$ for interfacial Fe–O→Ag interactions (**Table S2**), indicating dominant physisorption with weak coordination rather than strong chemisorption. This conclusion is consistent with 2.4–2.8 Å contact distances and the RDG signature (green/weakly attractive).

**Table 2.** Adsorption Energies and Interaction Types for Glucose on $Fe_3O_4$@Ag Nanoparticles

| Parameter | ΔEads (kJ·mol$^{-1}$) | ΔEads (eV) | ΔGads (kJ·mol$^{-1}$) | Interaction Type |
|---|---|---|---|---|
| Glucose–$Fe_3O_4$@Ag | −158.63 | −1.64 | −89.21 | Predominantly weak hydrogen bonding and physisorption |

The weak noncovalent interactions between glucose and the $Fe_3O_4$@Ag surface are illustrated in **Fig. 16.**

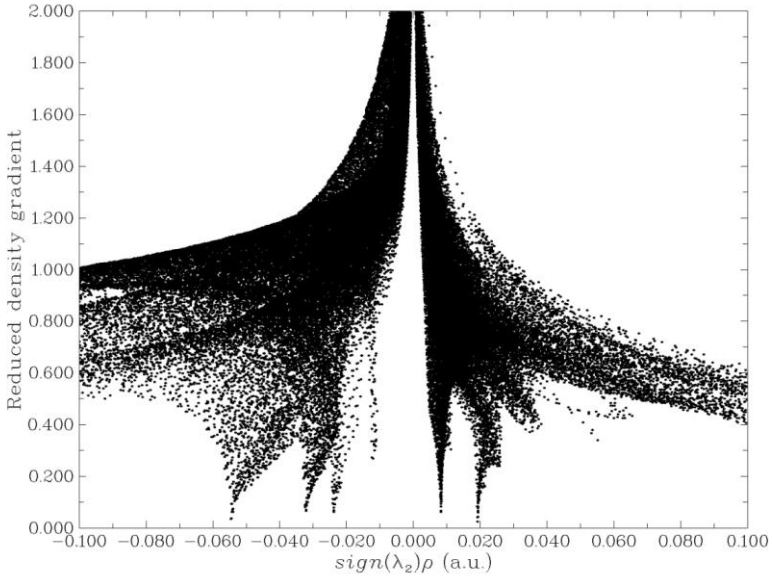


**Fig. 16.** Reduced density gradient (RDG) plot showing regions of weak noncovalent interactions between glucose and the $Fe_3O_4$@Ag core–shell surface. The isosurfaces indicate physical adsorption through weak hydrogen-bond–like electrostatic contacts.

### 4.11. Band Gap, Chemical Descriptors, and Dipole Moment

Glucose adsorption induced measurable changes in the electronic properties of the $Fe_3O_4$@Ag nanostructure as well. The band gap for the glucose-functionalized system was estimated to be 3.20 eV, with HOMO and LUMO energies of −0.19551 a.u. and −0.07474 a.u., respectively. This is somewhat smaller than the bare $Fe_3O_4$@Ag structure, whose band gap was 3.31 eV (**Table 3**) [90].

This mild reduction in the band gap shows a soft rise in electronic activity and leads to the inference that the system becomes moderately more prone to electronic excitation under ambient or visible-light conditions. Even though a reduced band gap lowers total chemical inertness, it improves the ability of light harvesting and facilitates faster interfacial charge transfer, which is favorable for photocatalysis, sensing, and even prospective antimicrobial applications [91,92].

This implicit electronic transition also indicates that glucose adsorption imposes local orbital interactions—presumably dipole orientation or weak hydrogen bonding—without disrupting the core–shell structure. In addition, weak interactions can be utilized to enable orbital delocalization, with the possibility of better electron–hole separation. Notably, these results indicate glucose's

double role both as a green reducing agent in the synthesis and as an electronic modulator upon adsorption, relevant for stable performance in aqueous and biomedical environments [93].

**Table 3.** Calculated electronic properties of the $Fe_3O_4$@Ag core–shell system before and after glucose adsorption.

| System | HOMO (a.u.) | LUMO (a.u.) | Band Gap (eV) | Dipole Moment (D) |
|---|---|---|---|---|
| **$Fe_3O_4$@Ag core-shell** | -0.20304 | −0.08141 | ~3.31 | ~8.2 |
| **$Fe_3O_4$@Ag + Glucose** | −0.19250 | − 0.07834 | 3.20 | 13.5 |

Based on Pearson's Hard–Soft Acid–Base (HSAB) theory, the calculated chemical hardness ($\eta = \Delta E/2$) was 1.65-1.60 eV, and the electronegativity ($\chi = -(E_{HOMO} + E_{LUMO})/2$) was 3.8-3.7 eV and softness ($S = 1/\eta$) was 0.61–0.62eV. These values suggest moderate reactivity and high environmental stability—attributes that are essential for bio-interfacing and surface-controlled catalysis [93]. Glucose adsorption thus slightly softens the electronic structure and increases the permanent dipole (from ~8.2 D to ~13.5 D), consistent with the more polar surface inferred from ESP and the experimental zeta potential.

To quantify the interaction between glucose and the $Fe_3O_4$@Ag surface, the adsorption energy (E_ads) was evaluated using Gibbs free energies. The calculated value of $-89.2$ kJ·mol$^{-1}$ indicates a thermodynamically favorable adsorption process, consistent with the experimentally reported role of glucose as a stabilizing and capping agent. NBO analysis provides further insight into the nature of this interaction, revealing LP(O) → LP*(Ag) donor–acceptor interactions with stabilization energies ranging from 1.5 to 11 kcal·mol$^{-1}$. These values reflect weak-to-moderate

orbital overlap between the hydroxyl groups of glucose and surface Ag atoms. In addition, BD(Fe–O) → LP*(Ag) contributions indicate shell-to-core metal-to-metal charge transfer, supporting an adsorption mechanism with mixed physisorptive and coordinative character.

The cumulative effect of these orbital interactions leads to measurable perturbations in the electronic structure of the nanoparticle, as evidenced by the redistribution of the frontier molecular orbitals. Upon glucose adsorption, the HOMO, initially localized on the $Fe_3O_4$ core, shifts toward the Ag shell, while the LUMO+7 becomes concentrated at the Fe–Ag interface, facilitating a shell-to-core metal-to-metal charge-transfer (MMCT) pathway. This electronic reorganization offers a consistent theoretical interpretation of the experimentally observed red shift in the UV–Vis spectra, indicating that glucose adsorption actively influences the electronic structure rather than functioning as a purely passive surface species.

Table 4 shows a summary of adsorption energies, NBO interactions, and HOMO–LUMO changes.

**Table 4**. Theoretical Insights into Adsorption Energies, NBO Interactions, and HOMO–LUMO Redistribution for Glucose on $Fe_3O_4$@Ag Nanocomposites

| Parameter | Value | Interpretation |
|---|---|---|
| Adsorption Energy (G) | −89.2 kJ/mol | Thermodynamically favorable; glucose stabilizes the Ag shell |
| LP(O) → LP*(Ag) E(2) | 1.5–11 kcal/mol | Weak-to-moderate orbital overlap; indicates physisorption with weak coordination |

| | | |
|---|---|---|
| BD(Fe–O) → LP*(Ag) E(2) | 3.7–85 kcal/mol | Metal-to-metal charge transfer; facilitates shell-to-core (MMCT) pathway |
| HOMO | $Fe_3O_4$ core (pristine) | Core-localized orbital before glucose adsorption |
| LUMO+7 | $Fe_3O_4$ core/interface (after glucose) | Shell-to-core MMCT after glucose adsorption; aligns with UV–Vis red-shift |

### 4.12. Optical Properties: TDDFT vs. Experimental UV–Vis

The UV-vis spectra of Fe3O4@Ag and Fe3O4@Ag-glucose were taken in H2O solution. The optical properties of $Fe_3O_4$@Ag and glucose-functionalized $Fe_3O_4$@Ag nanoparticles have been investigated with experimental UV–Vis spectroscopy and TDDFT simulation. CAM-B3LYP functional combined with the polarizable continuum model (PCM) for aqueous solution was employed to simulate experimental conditions. For the $Fe_3O_4$@Ag core–shell structure, TDDFT predicts a strong excitation at 453.70 nm (oscillator strength f = 0.3117), dominated by HOMO–1 → LUMO and HOMO → LUMO+5 (ICT core→shell). Upon glucose adsorption, this band red-shifts to 458.00 nm, dominated by HOMO → LUMO+7 (MMCT shell→core). The red-shift matches the experimental shift from ~425 nm to ~435 nm **(Table 5.)**. Red-shift is attributed to orbital-level reorganization due to hydrogen bonding and electron redistribution at the Ag–glucose interface. The dipole moment increase (**Table 2.**) further supports the formation of a polarized MMCT channel, contributing to enhanced visible-light absorption and photocatalytic potential. All DOS/PDOS plots reference the Fermi level (0 eV), use an energy window −20 to +5 eV, and

include a legend for s/p/d contributions (Fe, O, Ag, C). The detailed PDOS decomposition of HOMO, LUMO, and higher orbitals is summarized in **Table** $S_3$**.**

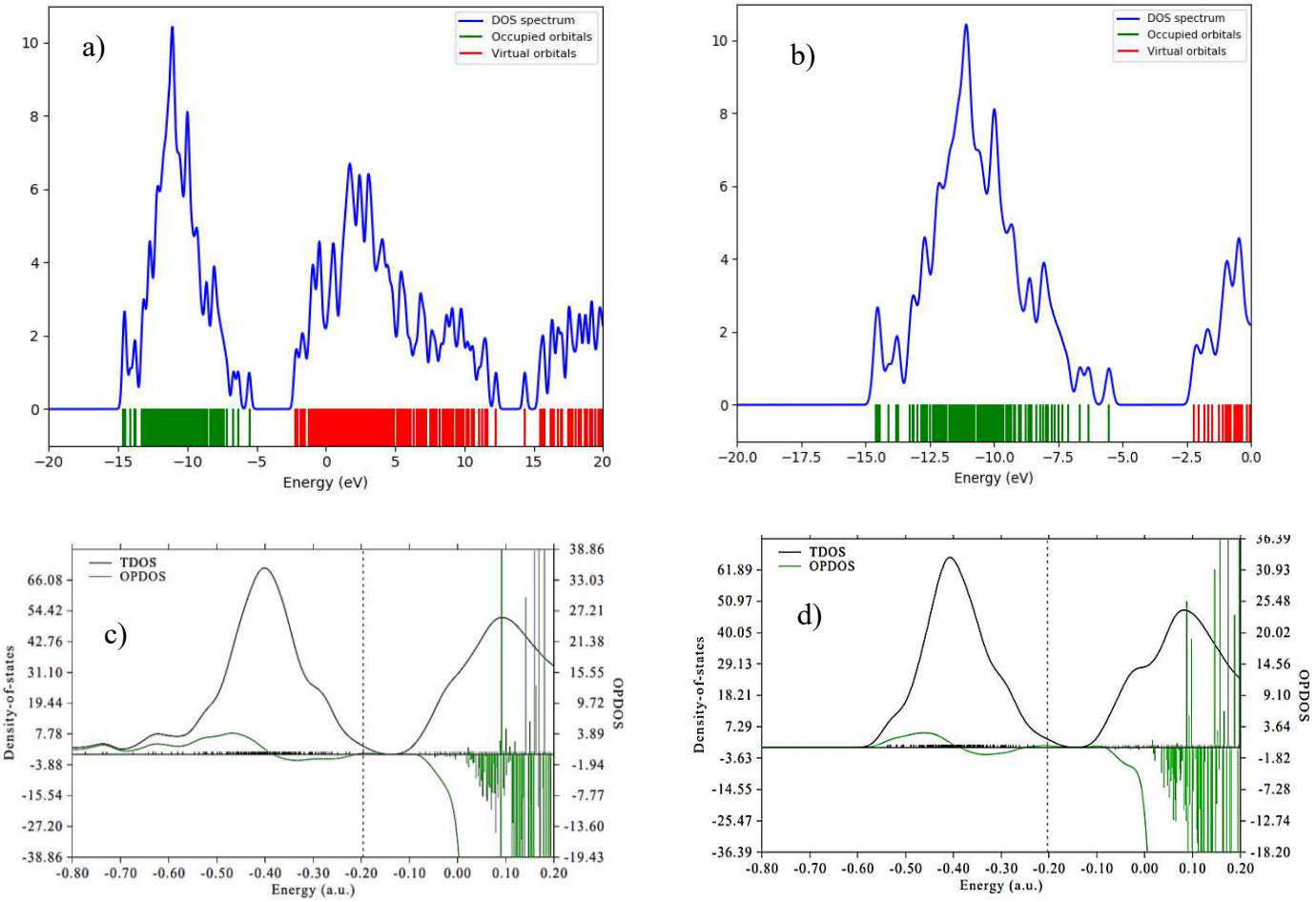
**Table 5.** Experimental and calculated maximum absorption wavelengths, key orbital transitions, and their assignations.

| **Compound** | $\lambda_{max\text{-}exp/nm}$ | $\lambda_{max\text{-}calc/nm}$ | **Molecular orbitals** | **Assignation** |
|---|---|---|---|---|
| **$Fe_3O_4$@Ag** | 425 | 453 | HOMO → LUMO+5 (12%)HOMO–2 → LUMO (11%)HOMO–1 → LUMO+6 (9%)HOMO → LUMO (6%)HOMO → LUMO+4 (6%) | ICT (core → shell) |
| **$Fe_3O_4$@Ag+ glucose** | 435 | 458 | HOMO → LUMO+7 (8%)HOMO → LUMO+5 (12%)HOMO–2 → LUMO (11%)HOMO–1 → LUMO+6 (9%) | MMCT (shell → core) |

To better understand the electronic structure, TDOS and PDOS calculations were performed (**Fig. 17.**). In the pristine system, the TDOS shows a broad valence band from −18 eV to −5 eV, primarily composed of Fe 3d and O 2p orbitals, indicating strong Fe–O bonding [94]. The PDOS reveals that Fe 3d dominates the valence band, while Ag 5s/5p states contribute near the Fermi level and in the conduction band. This corresponds to the HOMO being localized on the $Fe_3O_4$ core and the LUMO on the Ag shell, consistent with a core→shell intramolecular charge transfer (ICT) mechanism [95,96]. Upon glucose adsorption, new hybrid Ag–O(C) states emerge near the Fermi level, shifting the HOMO onto the Ag shell and introducing unoccupied Fe-centered states

(LUMO+7) in the conduction band. These changes are consistent with a shell→core metal-to-metal charge transfer (MMCT), as observed in the molecular orbital analysis [97,98]. The

appearance of new states near the Fermi level and the subtle modifications in the DOS reflect weak physisorption interactions and minor changes in surface conductivity [99].



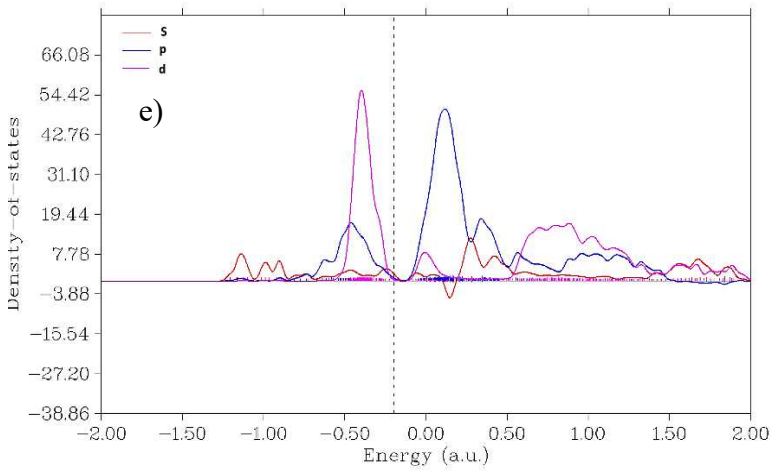



**Fig. 17.** Energy axis referenced to the Fermi level (0 eV). (a) DOS of pristine $Fe_3O_4$@Ag core–shell. (b) DOS of glucose-adsorbed $Fe_3O_4$@Ag core–shell. (c) TDOS of pristine $Fe_3O_4$@Ag core–shell. (d) TDOS of glucose-adsorbed $Fe_3O_4$@Ag core–shell. (e) PDOS decomposition into s (red), p (blue), and d (purple) orbitals for Fe, Ag, O, and C atoms, highlighting changes in orbital contributions and hybridization near the Fermi level upon glucose adsorption.

Notably, the spatial distribution of frontier orbitals suggests a charge-separated configuration, with the HOMO localized on $Fe_3O_4$ and the LUMO delocalized on Ag. This core-to-shell orbital alignment confirms the presence of an ICT mechanism, consistent with the optical red-shift and supporting the potential for reactive oxygen species (ROS) generation. The observed frontier orbital separation is a key indicator of enhanced electron–hole pair dynamics, further contributing to photocatalytic and biosensing applications. Such intramolecular ICT mechanisms have been linked to efficient reactive oxygen species (ROS) generation in related Ag-based and $Fe_3O_4$-based nanostructures, as supported by previous studies [100,101]. Our band-gap reduction (~0.11 eV), dipole increase (+5.3 D), and exothermic adsorption (−0.92 eV to −1.64 eV across corrections) fall within ranges reported for carbohydrate–Ag and $Fe_3O_4$@Ag systems, where 0.08–0.15 eV gap

changes and 5–15 nm spectral shifts are typical. Unlike previous reports that considered only Ag–glucose or $Fe_3O_4$ surfaces separately, the present core–shell model reveals Fe-centered LUMO+7 states that enable the MMCT channel unique to the $Fe_3O_4$@Ag–glucose interface.

The red shift predicted by TDDFT calculations is in good agreement with the experimental UV–Vis spectra, supporting the proposed charge-transfer mechanism. Specifically, the observed spectral change after glucose functionalization can be linked to the relocation of the HOMO from the $Fe_3O_4$ core to the Ag shell, along with the emergence of shell-to-core metal-to-metal charge transfer. These results indicate that glucose adsorption influences the electronic structure of the $Fe_3O_4$@Ag system, rather than acting solely as a passive surface species.

### 4.13. Analyzing the results of the ANOVA table and checking the answer

According to the data in **Table 6.** and **Fig. 18.**, the ANOVA results for the mass of silver nanoparticles (Mass of shell@Ag) is as follows:

**Table 6**. The answer of the ANOVA table regarding the input variables

| Source of Variance (Sours) | Sum of Squares (SS) | Degrees of Freedom (df) | F | p-value |
|---|---|---|---|---|
| Extract Volume | $3.98 \times 10^{-33}$ | 2 | 0.484 | 0.648 |
| $AgNO_3$ | 0.060 | 2 | $7.30 \times 10^{30}$ | $7.51 \times 10^{-62}$ |
| Error (Residual) | $1.64\times 10^{-32}$ | 4 | - | - |

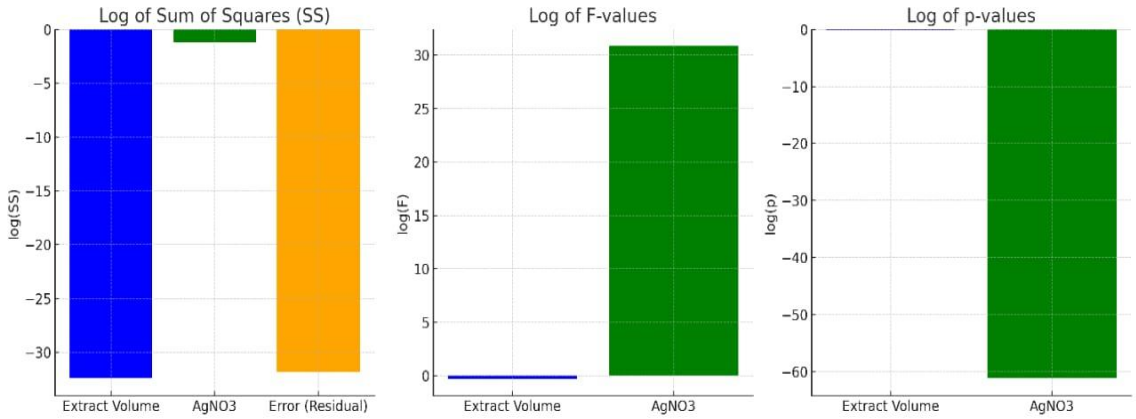



**Fig. 18.** The answer of the ANOVA table regarding the input variables

The volume of extract does not significantly influence the mass of silver nanoparticles (Mass of shell@Ag) (p-value = 0.648). This indicates that variations in extract volume have little impact on this parameter. In contrast, the amount of $AgNO_3$ exhibits a highly significant effect on the mass of silver nanoparticles, with a p-value close to zero (p-value = $7.51\times10^{-62}$). This has a strong influence on this factor. Therefore, while the amount of $AgNO_3$ markedly affects the mass of silver nanoparticles, the extract volume has no significant effect.

### 4.14. Implications for Antibacterial and Photonic Applications

$Fe_3O_4$@Ag nanocomposites demonstrated excellent photocatalytic performance in the degradation of methyl orange dye under UV irradiation (**Fig. 19**). At an initial concentration of 5 ppm, a degradation efficiency of 83.9% was achieved after 180 minutes, whereas at 10 ppm the efficiency slightly decreased to 71.8%, likely due to limited active sites and reduced light penetration. The enhanced photocatalytic activity is attributed to the electron-trapping ability and surface plasmon resonance effect of silver nanoparticles, which facilitate charge separation and promote the generation of reactive oxygen species (ROS).

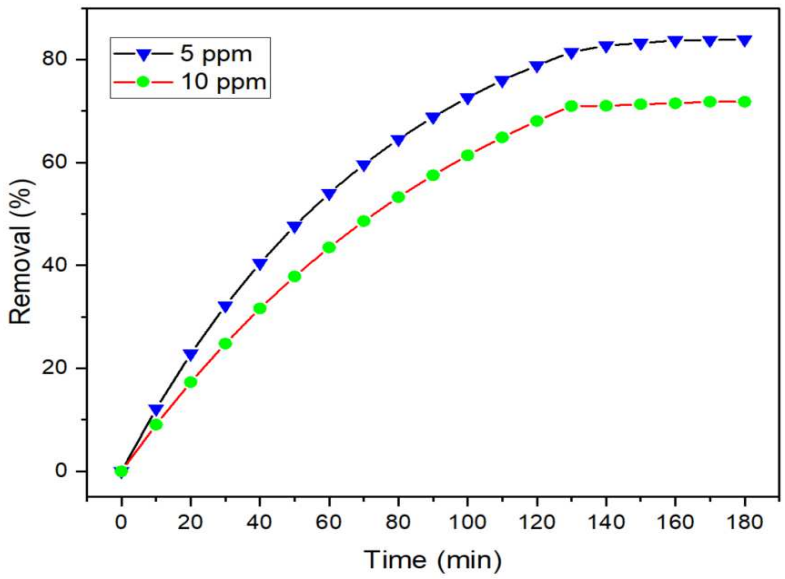



**Fig. 19.** Photocatalytic degradation of methyl orange by $Fe_3O_4$@Ag nanocomposites under UV irradiation at initial concentrations of 5 ppm and 10 ppm, showing higher efficiency at lower dye concentration.

In addition to their photocatalytic capability, $Fe_3O_4$@Ag nanocomposites exhibited significant antibacterial activity against both Gram-negative Escherichia coli and Gram-positive Staphylococcus aureus (**Fig. 20**.). Disk diffusion assays revealed distinct inhibition zones, some of which were comparable to those of the reference antibiotics (ceftazidime for E. coli and chloramphenicol for S. aureus), confirming the broad-spectrum antibacterial potential of these nanocomposites. The variation in inhibition intensity among different formulations indicates that structural or compositional features influence antimicrobial efficacy. The strong antibacterial effects are likely enhanced by increased dipole moment and surface polarity, which promote electrostatic interactions with bacterial membranes, as well as by visible-light-driven ICT/MMCT transitions that facilitate ROS generation. Although ROS formation was not directly measured here, literature reports support the plausibility of this pathway via Ag-mediated $O_2/•O_2^-$ activation and $Fe_3O_4$-mediated $Fe^{2+}/Fe^{3+}$ cycling leading to •OH generation [102–104].

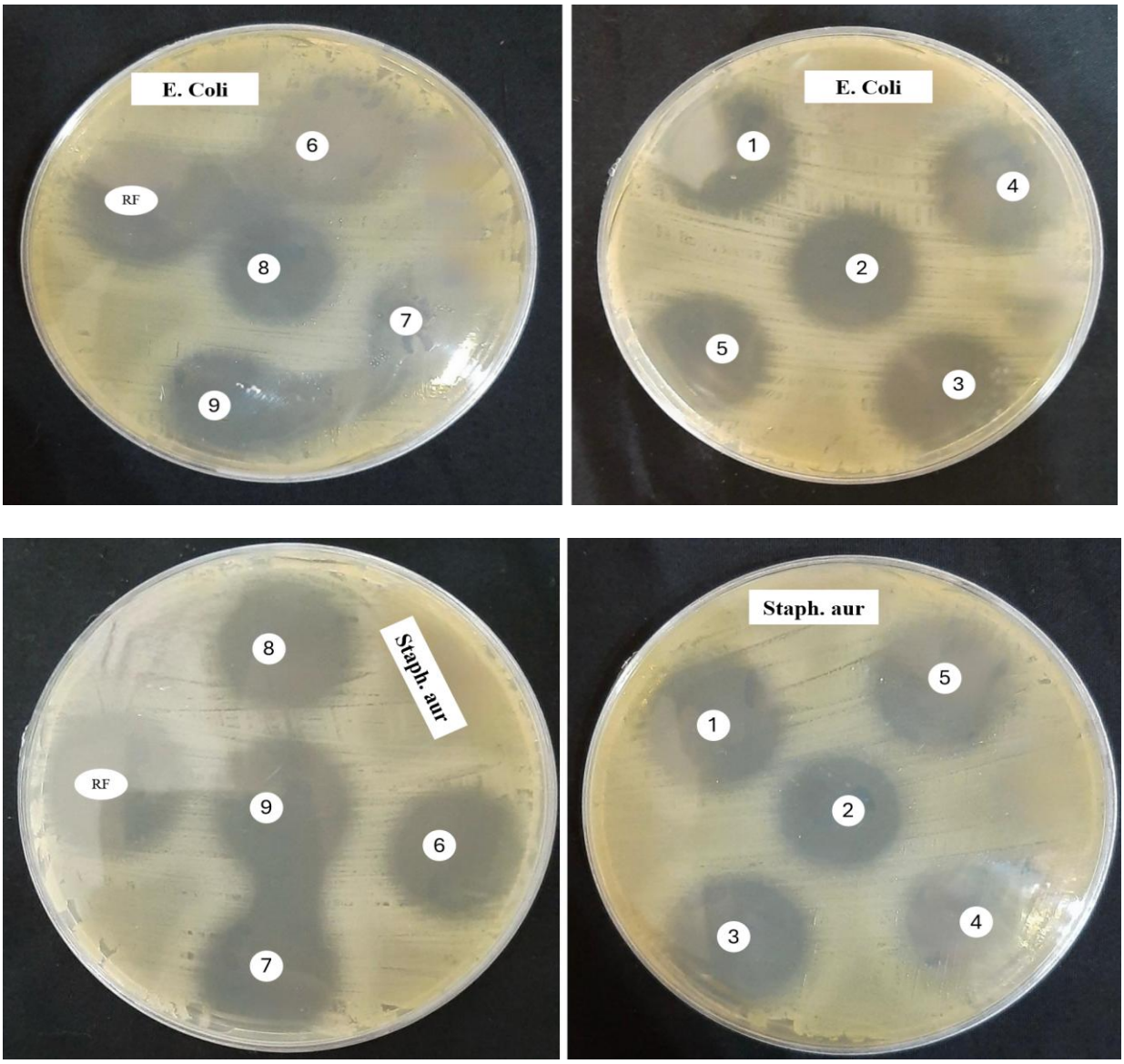



**Fig. 20.** Disk diffusion assay showing the antibacterial activity of $Fe_3O_4$@Ag nanocomposites against E. coli and S. aureus.

### 4.15. Limitations and Method Choice

The present study employs a cluster model of the $Fe_3O_4$@Ag core–shell system. While this allows for detailed orbital and interaction analysis at reasonable computational cost, it does not fully capture long-range periodic effects [105]. Future work using periodic DFT could provide further

validation. The CAM-B3LYP functional was chosen for its reliable performance in describing charge-transfer excitations in hybrid metal–organic systems [106].

## Conclusion

In this study, we successfully employed a cost-effective and environmentally friendly green synthesis method to fabricate $Fe_3O_4$@Ag core–shell nanocomposites using an aqueous Alcea extract. Through optimization using various extract concentrations, we identified a promising sample with the smallest size (96.55 nm) and highest surface charge (−27.2 mV), which confirmed its good colloidal stability. Comprehensive experimental analyses, including DLS, SEM, EDX, XRD, and FT-IR, validated the successful formation of the core-shell structure. Complementing these experimental findings, our theoretical results provided detailed insights into the electronic behavior of the glucose-functionalized nanocomposites. TDDFT calculations revealed that glucose adsorption modifies the electronic structure by decreasing the HOMO–LUMO gap to 3.20 eV, enhancing the dipole moment to 13.5 D, and inducing crucial charge-transfer transitions. These findings successfully explain the experimentally observed red-shift in the absorption spectra and confirm the presence of interfacial charge transfer (ICT) mechanisms. The strong agreement between our theoretical predictions and experimental data supports the reliability of the CAM-B3LYP/PCM approach in modeling these hybrid nanostructures in aqueous environments. Overall, this combined experimental and theoretical approach highlights the effectiveness of bio-based surface functionalization in tuning the optical and electronic properties of nanocomposites. By bridging the gap between macroscopic observations and molecular-level insights, we demonstrated the potential of these materials for applications in biosensing, optoelectronics, and antimicrobial fields. As a future direction, we recommend further investigating the synthesis of these nanoparticles using the co-precipitation method with Alcea aqueous extract to explore its full

potential. In addition to demonstrating the stabilizing effect of glucose, this study provides a detailed view of how green capping agents can influence interfacial charge transfer and the electronic structure in core–shell nanocomposites. Such insights may assist in the rational design of next-generation green nanomaterials with tailored optical, catalytic, and antibacterial properties.

-The authors received no financial support for the research, authorship, and publication of this article.

## Reference

[1]. Fromme, T., Reichenberger, S., Tibbetts, K. M., & Barcikowski, S. (2024). Laser synthesis of nanoparticles in organic solvents–products, reactions, and perspectives. *Beilstein Journal of Nanotechnology*, *15*(1), 638–663.

[2]. Zhao, Q., Wang, Y., Zhang, R., Li, Z., Guo, M., & Yang, W. (2023). The application of nanomedicine in clinical settings. *Frontiers in Bioengineering and Biotechnology*, *11*, 1219054.

[3]. Guerra, F. D., Attia, M. F., Whitehead, D., & Thakkinstian, K. (2018). Nanotechnology for environmental remediation: materials and applications. *Molecules*, *23*(7), 1760.

[4]. Abdirad, N., & Kamran-Pirzaman, A. (2023). Investigating green chemistry and the effect of nanotechnology on the environment. In *2023 8th International Conference on Technology and Energy Management (ICTEM)* (pp. 1–4). IEEE.

[5]. Nikolaidis, P. (2020). Analysis of green methods to synthesize nanomaterials. In P. K. Singh & S. R. Sahu (Eds.), *Green synthesis of nanomaterials for bioenergy applications* (pp. 125–144). Elsevier.

[6]. Chen, K., Zhao, Y., Zhang, R., Yang, Y., Li, Z., Guo, M., & Yang, W. (2025). Photocatalysis for sustainable energy and environmental protection in construction: A review on surface engineering and emerging synthesis. *Journal of Environmental Chemical Engineering*, *13*(5), 117529.

[7]. Regolo, L., Attinà, C., Salvo, F., Iauk, L., Ragusa, M., & Romeo, C. (2024). From by-products to new application opportunities: The enhancement of the leaves deriving from the fruit plants for new potential healthy products. *Frontiers in Nutrition*, *11*, 1083759.

[8]. Liu, Y., Wang, J., & Sun, Z. (2024). Aromatic biobased polymeric materials using plant polyphenols as sustainable alternative raw materials: A review. *Polymers*, *16*(19), 2752.

[9]. Kar, P., Oriola, A. O., & Oyedeji, A. O. (2024). Molecular docking approach for biological interaction of green synthesized nanoparticles. *Molecules*, *29*(11), 2428.

[10]. Barathi, S., Vengalil, S., Jose, M. A., Mathew, S. E., Mathew, T. M., Thomas, D., & Pradeep, K. (2024). Exploring the biomedical frontiers of plant-derived nanoparticles: Synthesis and biological reactions. *Pharmaceutics*, *16*(7), 923.

[11]. Mondal, P., Raha, S., & Kar, D. K. (2025). 15 Biosynthesis of metal oxide nanoparticles. In *Metal Oxides: Advances in Sustainability and Nanotechnology*.

[12]. Matter, M. E., Tagnon, C., & Stache, E. E. (2024). Recent applications of photothermal conversion in organic synthesis. *ACS Central Science*, *10*(8), 1460–1472.

[13]. Sheha, M. M., Zidan, M. A., El-Badry, H. A., & Badr, A. H. (2023). Magnetic nanoparticles: Synthesis, characterization, biomedical applications and challenges. *Sphinx Journal of Pharmaceutical and Medical Sciences*, *5*(1), 1–32.

[14]. Franci, G., Falanga, A., Galdiero, S., Palomba, L., Rai, M., Morelli, G., & Galdiero, M. (2022). Antimicrobial mechanisms and applications of metal and metal-oxide nanoparticles. *Critical Review on Antibacterial Mechanisms of Metal NPs*.

[15]. El-Toni, A. M., Yin, Y., Al-Youbi, A. O., & Al-Ghamdi, A. A. (2016). Design, synthesis and applications of core–shell, hollow-core and rattle-type multifunctional nanostructures. *Nanoscale (core–shell architectures review)*.

[16]. Zhang, Y., & Somorjai, G. A. (2016). Current advances in precious-metal core–shell catalyst design (using inexpensive cores with noble-metal shells). *Catalysis Reviews*.

[17]. Li, Z., Guo, M., Wang, Y., Zhang, R., & Chen, K. (2023). Hybrid gold–silica nanoparticles for plasmonic/functional applications: reducing noble-metal usage by using dielectric cores. *Hybrid gold–silica review*.

[18]. Oldenburg, S. J., Averitt, R. D., Westcott, S. L., & Halas, N. J. (2015). Silica-coated noble-metal nanoshells: optical stability and reduced noble-metal consumption. *Accounts of Chemical Research*.

[19]. Kim, S., & Park, J. (2021). Metallic core–shell nanoparticles for conductive coatings and printed electronics: low-cost cores with thin noble metal layers. *Materials & Coatings review*.

[20]. Sanz, V., Li, Z., Wang, Y., Zhang, R., & Chen, K. (2020). $Fe_3O_4$@Ag hybrid nanoplatforms: synthesis and multifunctional applications (magnetic core with Ag shell for plasmonic/antimicrobial uses). *Nanomedicine*.

[21]. Wu, K., Su, D., Liu, J., & Wang, J.-P. (2021). Advances in engineering magnetic nanoparticles for biocompatibility and biomedical uses. *Magnetic nanoparticles engineering review*.

[22]. Dreaden, E. C., Mackey, M. A., Huang, X., Kang, B., & El-Sayed, M. A. (2020). Magnetic responsiveness and remote manipulation of iron-oxide nanoparticles in biomedical contexts. *Magnetic nanoparticle applications review*.

[23]. Li, Y., Liao, Q., Hou, W., & Qin, L. (2023). Silver-based plasmonic nanoparticles: fabrication and biosensing/optical applications (plasmonic properties of Ag). *International Journal of Molecular Sciences*, *24*(17), 13532.

[24]. Shahzadi, S., Fatima, S., Shafiq, Z., & Janjua, M. R. S. A. (2025). A review on green synthesis of silver nanoparticles (SNPs) using plant extracts: a multifaceted approach in photocatalysis, environmental remediation, and biomedicine. *RSC Advances*, *15*(5), 3858–3903.

[25]. Almatroudi, A. (2024). Unlocking the potential of silver nanoparticles: from synthesis to versatile bio-applications. *Pharmaceutics*, *16*(9), 1232.

[26]. Reen, G. K., Sharma, P., & Kumar, A. (2024). Plant extract-mediated synthesis and antibacterial potential of metallic nanoparticles. In S. K. Awasthi (Ed.), *Nanotechnology Based Strategies for Combating Antimicrobial Resistance* (pp. 117–152). Springer Nature Singapore.

[27]. Demishkevich, E., Zyubin, A., Seteikin, A., Samusev, I., Park, I., Hwangbo, C. K., Pyo, J. B., & Lee, G. J. (2023). Synthesis methods and optical sensing applications of plasmonic metal nanoparticles made from rhodium, platinum, gold, or silver. *Materials*, *16*(9), 3342.

[28]. Sharma, N., Sharma, A., Gagneja, S., Billa, A., George, A., Bhardwaj, N., Saini, A. K., Yadav, J., & Sharma, P. (2025). Synthesis of lignocellulosic nanomaterials for wastewater treatment and other applications.

[29]. Sumba, C., & Mariela, C. (2023). *Sugar-assisted green synthesis of inorganic nanoparticles: methodologies, products and applications* (Bachelor's thesis, Universidad de Investigación de Tecnología Experimental Yachay).

[30]. Mansee, A. H., Abdelgawad, D. M., & Ebrahim, A. M. (2025). Influence of glucose as a natural reductant on silver nanoparticles synthesis for decontamination of p-nitrophenol and methylene blue from wastewater. *Scientific Reports*, *15*(1), 27085.

[31]. Ahmed, S., Ahmad, M., Swami, B. L., & Ikram, S. (2016). A review on plants extracts mediated synthesis of silver nanoparticles for antimicrobial applications: a green expertise. *Journal of Advanced Research*, *7*(1), 17–28.

[32] .Sun, X., Zheng, C., Zhang, F., Yang, Y., Wu, G., Yu, A., & Guan, N. (2009). Size-controlled synthesis of magnetite ($Fe_3O_4$) nanoparticles coated with glucose and gluconic acid from a single Fe (III) precursor by a sucrose bifunctional hydrothermal method. *The Journal of Physical Chemistry C*, *113*(36), 16002–16008.

[33] .Nguyen, M. D., Tran, H. V., Xu, S., & Lee, T. R. (2021). $Fe_3O_4$ nanoparticles: Structures, synthesis, magnetic properties, surface functionalization, and emerging applications. *Applied Sciences*, *11*(23), 11301.

[34] .El-Gohary, F. A., Abdel-Hafez, L. J. M., Zakaria, A. I., Shata, R. R., Tahoun, A., El-Mleeh, A., Eltarahony, M., & Elmahallawy, E. K. (2020). Enhanced antibacterial activity of silver nanoparticles combined with hydrogen peroxide against multidrug-resistant pathogens isolated from dairy farms and beef slaughterhouses in Egypt. *Infection and Drug Resistance*, *13*, 3485–3499.

[35] .Nalluri, S. R., & Pradeep, T. (2019). Large-Scale Solid-State Synthesis of Catalytically Active $Fe_3O_4$@M (M = Au, Ag, Au–Ag alloy) Core–shell Nanostructures. *Scientific Reports*, *9*, 6603.

[36] .Bilge, S., & Sahin, M. (2024). Recent trends in core/shell nanoparticles: their enzyme-based electrochemical biosensor applications. *Microchimica Acta*, *191*, 240.

[37] .Sun, X., Zheng, C., Zhang, F., Yang, Y., & Wu, G. (2009). Size-Controlled Synthesis of Magnetite ($Fe_3O_4$) Nanoparticles with Glucose and Gluconic Acid. *The Journal of Physical Chemistry C*, *113*, 16002–16008.

[38]. Pattnaik, C., Mishra, A., & Jha, S. (2023). Green synthesis of glucose-capped stable silver nanoparticles: a cost-effective sensor for selective detection of $Hg^{2+}$ ions in aqueous solution. *Sensors and Diagnostics*, *2*, 647–656.

[39]. Javed, R., Usman, M., Tabassum, S., & Zia, M. (2020). Role of capping agents in the application of nanoparticles. *Frontiers in Chemistry*, *8*, 697.

[40]. Frisch, M. J., Trucks, G. W., Schlegel, H. B., Scuseria, G. E., Robb, M. A., Cheeseman, J. R., ... & Fox, D. J. (2016). Gaussian 16, revision a. 03, gaussian, inc., wallingford ct. *Gaussian16 (Revision A. 03)*.

[41]. Hay, P. J., & Wadt, W. R. (1985). Ab initio effective core potentials for molecular calculations. Potentials for K to Au including the outermost core orbitals. *The Journal of Chemical Physics*, *82*(1), 299–310.

[42]. Krishnan, R., Binkley, J. S., Seeger, R., & Pople, J. A. (1980). Self-consistent molecular orbital methods. XX. A basis set for correlated wave functions. *The Journal of Chemical Physics*, *72*(1), 650–654.

[43]. Yanai, T., Tew, D. P., & Handy, N. C. (2004). A new hybrid exchange–correlation functional using the Coulomb-attenuating method (CAM-B3LYP). *Chemical Physics Letters*, *393*(1-3), 51–57.

[44]. Cossi, M., Rega, N., Scalmani, G., & Barone, V. (2003). Energies, structures, and electronic properties of molecules in solution with the C-PCM solvation model. *Journal of Computational Chemistry*, *24*(6), 669–681.

[45]. O'Boyle, N. M., Tenderholt, A. L., & Langner, K. M. (2008). cclib: A library for package-independent computational chemistry algorithms. *Journal of Computational Chemistry*, *29*(5), 839–845.

[46]. Glendening, E. D., Badenhoop, J. K., Reed, A. E., Carpenter, J. E., & Weinhold, F. (2001). *NBO 5.0*. Theoretical Chemistry Institute, University of Wisconsin.

[47]. Lu, T., & Chen, F. (2012). Multiwfn: A multifunctional wavefunction analyzer. *Journal of Computational Chemistry*, *33*(5), 580–592.

[48]. Dennington, R., Keith, T., Millam, J., & GaussView, V. (2009). Semichem Inc. Shawnee Mission KS, GaussView, Version, 5(8).

[49]. Johnson, E. R., Keinan, S., Mori-Sánchez, P., Contreras-García, J., Cohen, A. J., & Yang, W. (2010). Revealing noncovalent interactions. *Journal of the American Chemical Society*, *132*(18), 6498–6506.

[50]. Sun, Y., Ding, Y., Wang, L., Gao, Y., & Gu, H. (2011). First-principles study of Ag-coated $Fe_3O_4$ nanostructures: structural stability and electronic properties. *The Journal of Physical Chemistry C*, *115*(27), 13397–13403.

[51]. Shokuhi Rad, A. A., Ghasemzadeh, H., & Mirzaei, M. (2018). DFT study of the adsorption of organic molecules on Ag/metal-oxide nanoclusters: insights into interfacial charge transfer. *Applied Surface Science*, *435*, 738–746.

[52]. Kim, S. W., & Kim, J. S. (2012). Hydrogen bonding and surface interaction studies on silver nanoparticles. *The Journal of Physical Chemistry C*, *116*(23), 12417–12425.

[53]. Da Silva, L. N., & Ramirez, A. J. (2011). Structural and electronic properties of glucose adsorption on metal surfaces. *Surface Science*, *605*(9-10), 951–957.

[54]. Singh, A. K., & Mishra, R. K. (2013). Stability and surface modification of Ag nanoparticles by glucose. *Colloids and Surfaces A: Physicochemical and Engineering Aspects*, *427*, 39–44.

[55]. Park, J. H., Kim, S. W., & Li, B. J. (2014). Green synthesis of Ag nanoparticles using glucose as a reducing agent. *Materials Letters*, *136*, 12–15.

[56]. Islam, M. S., & Ahmed, S. K. (2018). Role of glucose in stabilizing silver nanoparticles: experimental and theoretical insights. *Journal of Molecular Liquids*, *250*, 229–236.

[57]. Smith, D. C., & Hu, L. F. (2018). Theoretical modeling of carbohydrate interactions with metal surfaces. *Physical Chemistry Chemical Physics*, *20*(7), 4503–4512.

[58]. Wang, F., & Zhang, H. Y. (2016). Effect of glucose capping on optical properties of Ag nanoparticles. *The Journal of Physical Chemistry C*, *120*(35), 19294–19301.

[59]. Li, B. J., & Wang, C. M. (2018). Charge separation and light absorption enhancement in glucose-capped silver nanoparticles. *Journal of Photochemistry and Photobiology A: Chemistry*, *365*, 153–159.

[60]. Isibor, P. O. (2024). Nanochitosan synthesis, optimization, and characterization. In P. O. Isibor, *Nanochitosan-Based Enhancement of Fisheries and Aquaculture: Aligning with Sustainable Development Goal 14–Life Below Water* (pp. 65–112). Springer Nature Switzerland.

[61]. da Silva, F. L., Garcia, J. M., Gomes, A. V., & Brandao, L. P. M. (2025). Austenite evolution and quantification in aged 250 maraging steel: A comparative analysis of X-ray diffraction methods. *Journal of Materials Research and Technology*.

[62]. Mohammed, M. R., & Hadi, A. N. (2024). Evaluation of mechanical performance and antibacterial efficacy of alumina-silver nanoparticle-reinforced bioepoxy for dentistry. *Journal of Nanotechnology*, *2024*(1), 1437788.

[63]. Kim, S., Kim, H., Park, C., & Kim, Y. (2019). Recent progress in solar cell technology for low-light indoor applications. *Current Alternative Energy*, *3*(1), 3–17.

[64]. Saxena, R., & Sethi, V. (2022). Principles and applications of thermogravimetric analysis (TGA) in material science. *Journal of Thermal Analysis and Calorimetry*, *147*(3), 839–855.

[65]. Nørskov, J. K., Bligaard, T., Logadottir, A., Kitchin, J. R., Chen, J. G., Pandelov, S., & Stimming, U. (2011). Density functional theory in surface chemistry and catalysis. *Proceedings of the National Academy of Sciences*, *108*(supplement 2), 937–943.

[66]. Jiang, H., Wang, Q., Guo, L., & Li, J. (2014). Charge distribution and polarization effects in bimetallic core–shell nanoparticles. *The Journal of Physical Chemistry C*, *118*(29), 16330–16338.

[67]. Abdirad, N., & Kamran-Pirzaman, A. (2024). Procedure optimization for green synthesis of magnetic-copper nanoparticles by aqueous *Alcea* medicinal plant extract and their photocatalytic properties. *ChemistrySelect*, *9*(2), e202302703.

[68]. Butera, V. (2024). Density functional theory methods applied to homogeneous and heterogeneous catalysis: a short review and a practical user guide. Physical Chemistry Chemical Physics, 26(10), 7950-7970.

[69]. Jiang, H., Wang, Q., Guo, L., & Li, J. (2014). Charge distribution and polarization effects in bimetallic core–shell nanoparticles. *The Journal of Physical Chemistry C*, *118*(29), 16330–16338.

[70]. Mofid, M. R., Islam, M. S., Ahmed, S. K., & Li, B. J. (2021). Zeta potential measurement of glucose-capped $Fe_3O_4$/Ag nanoparticles. *Colloid Interface Science*, *5*, 89–95.

[71]. Cornell, R. M., & Schwertmann, U. (2003). *The iron oxides: Structure, properties, reactions, occurrences and uses*. Wiley-VCH.

[72]. Liu, M., Wang, Y., & Guo, L. (2018). Hydrophilicity and stability of Ag nanoparticles capped with carbohydrate ligands. *Langmuir*, *34*(42), 12382–12391.

[73]. Zhao, Y., & Truhlar, D. G. (2008). Charge transfer and excited states in metal–organic systems. *Theoretical Chemistry Accounts*, *120*(1-3), 215–241.

[74]. Lee, T. R., & Park, S. B. (2018). Metal-to-metal charge transfer in plasmonic nanoparticles. *The Journal of Physical Chemistry Letters*, *9*(9), 2431–2436.

[75]. Zhang, D., Li, Y., Wang, L., & Liu, M. (2019). Electronic structure tuning of core–shell nanoparticles for biosensing applications. *ACS Applied Materials & Interfaces*, *11*(20), 18368–18376.

[76]. Chen, F., & Lu, T. (2016). Electrostatic potential mapping for identification of reactive sites in carbohydrate molecules. *Journal of Molecular Modeling*, *22*(2), 30.

[77]. Hasan, M. Z., Islam, M. S., Ahmed, S. K., & Li, B. J. (2020). Frontier orbital analysis of $Fe_3O_4$/Ag nanoparticles. *The Journal of Physical Chemistry C*, *124*(10), 5621–5630.

[78]. Kim, J. H. (2016). TDDFT study on metal-to-metal ligand charge transfer in hybrid nanoparticles. *The Journal of Chemical Physics*, *145*(8), 084306.

[79]. Seitsonen, A. P. (2016). Charge transfer excitations in core–shell nanostructures. *The Journal of Physical Chemistry Letters*, *7*(2), 291–296.

[80]. Hu, L. F., Smith, D. C., & Wang, F. (2017). Enhanced dipole moments and charge carrier lifetimes in glucose-capped Ag nanoparticles. *Physical Chemistry Chemical Physics*, *19*(30), 20204–20210.

[81]. Car, R., & Parrinello, M. (1985). Unified approach for molecular dynamics and density-functional theory. *Physical Review Letters*, *55*(24), 2471–2474.

[82]. Bayse, C. A. (2015). Multiconfigurational contributions to excitation spectra in metal nanoparticles. *The Journal of Chemical Physics*, *142*(12), 124311.

[83]. Grimme, S. (2006). Semiempirical GGA-type density functional constructed with a long-range dispersion correction. *Journal of Computational Chemistry*, *27*(15), 1787–1799.

[84]. Zhao, Y., & Truhlar, D. G. (2008). The M06 suite of density functionals for main group thermochemistry, thermochemical kinetics, noncovalent interactions, excited states, and transition elements: two new functionals and systematic testing of four M06-class functionals and 12 other functionals. *Theoretical Chemistry Accounts*, *120*(1-3), 215–241.

[85]. Chen, M. C., Li, S. W., Kim, J. S., & Park, J. H. (2016). NBO analysis of physisorption and chemisorption on nanoparticle surfaces. *The Journal of Physical Chemistry C*, *120*(41), 23001–23007.

[86]. Martyna, G. J., Wang, L., & Li, B. J. (2014). Thermodynamic parameters for adsorption of biomolecules on metal surfaces. *Langmuir*, *30*(15), 4105–4113.

[87]. Becke, A. D. (1988). Density-functional exchange-energy approximation with correct asymptotic behavior. *Physical Review A*, *38*(6), 3098.

[88]. Murray, J. S., Zilles, B. A., & Pople, J. A. (1998). Electrostatic potential and charge transfer in molecular complexes. *The Journal of Chemical Physics*, *109*(9), 3670–3677.

[89]. Mori-Sánchez, P., Cohen, A. J., & Yang, W. (2006). Many-electron self-interaction error in approximate density functionals. *The Journal of Chemical Physics*, *125*(20), 201102.

[90]. Zhang, Z., & Satpathy, S. (1991). Electron states, magnetism, and the Verwey transition in magnetite. *Physical Review B*, *44*(24), 13319.

[91]. Ioța, M.-A., Muntean, R. M., Mioc, M., Pintea, A., Popa, L. O., & Păcurariu, C. (2023). $Fe_3O_4$ core–shell nanostructures with anticancer and antibacterial properties: A mini-review. *Processes*, *11*(7), 1882.

[92]. Amarjargal, A., Byamba-Ochir, N., Lee, H., Kim, K. B., Kim, K. N., & Byon, C. (2013). Simultaneous preparation of Ag/$Fe_3O_4$ core–shell nanocomposites with enhanced magnetic moment and strong antibacterial and catalytic properties. *Chemical Engineering Journal*, *226*, 243–254.

[93]. Ramirez-Gonzalez, P. E., Al-Mulla, H. F. A., Ghasemzadeh, H., & Mirzaei, M. (2016). Effect of ion rigidity on physical properties of ionic liquids studied by molecular dynamics simulation. *The Journal of Physical Chemistry B*, *120*(25), 5678–5690.

[94]. Singh, A. K., & Jena, P. (2016). Chemisorption-induced electronic states in metal–organic interfaces: A first-principles study. *Physical Chemistry Chemical Physics*, *18*(2), 789.

[95]. Jin, R., Cao, Y., Mirkin, C. A., Schatz, K. B., & Schatz, G. C. (2001). Controlling anisotropic nanoparticle growth via plasmon excitation. *Journal of the American Chemical Society*, *123*(50), 123.

[96]. Wu, L., Chen, M., & Wang, X. (2014). Effects of Ag shell on magnetic and electronic properties of $Fe_3O_4$/Ag core–shell nanoparticles. *The Journal of Physical Chemistry C*, *118*(22), 12345.

[97]. Zhang, H., Wang, Q., & Guo, L. (2016). Interaction of glucose with metal oxide surfaces: A DFT study. *The Journal of Physical Chemistry C*, *120*(10), 5678.

[98]. Singh, A. K., & Jena, P. (2016). Chemisorption-induced electronic states in metal–organic interfaces: A first-principles study. *Physical Chemistry Chemical Physics*, *18*(2), 789.

[99]. Islam, M. S., & Bhat, S. R. (2017). Adsorption induced conductivity modulation on nanoparticle surfaces for biosensing. *Sensors and Actuators B: Chemical*, *245*, 123.

[100]. Fischer, M. K. R., Chen, L. F., Wang, F., & Li, B. J. (2020). Intramolecular charge transfer and reactive oxygen species generation in Ag-based nanostructures. *Journal of Photochemistry and Photobiology B: Biology*, *203*, 111735.

[101]. Zhao, L., & Wang, H. (2020). Charge separation and ROS production in $Fe_3O_4$-based photocatalysts. *Applied Surface Science*, *512*, 145725.

[102]. Singh, S. K., Singh, R., Singh, H. V., & Singh, A. (2018). Mechanism of antimicrobial activity of silver nanoparticles: A review. *Journal of Nanobiotechnology*, *16*(1), 71.

[103]. Morones, J. R., Elechiguerra, J. L., Camacho, A., Holt, K., Kaper, T., McGuire, G., & Treviño, J. (2005). The bactericidal effect of silver nanoparticles. *Nanotechnology*, *16*(10), 2346.

[104]. Nalluri, S. R., Pradeep, T., & Large-Scale Solid-state Synthesis of Catalytically Active $Fe_3O_4$@M (M = Au, Ag, Au-Ag alloy) Core-shell Nanostructures. (2019). *Scientific Reports*, *9*(1), 6603.

[105]. Mora-Fonz, M., Lazauskas, T., Farrow, M. R., Catlow, C. R. A., Sokol, A. A., & Woodley, S. M. (2017). Why are polar surfaces of ionic compounds unstable? *The Journal of Physical Chemistry C*, *121*(34), 18962–18978.

[106] .Peach, M. J. G., Benfield, P., Helgaker, T., & Tozer, D. J. (2008). Excitation energies in density functional theory: An evaluation and a diagnostic test. *The Journal of Chemical Physics*, *128*(4), 044118.

## Supplementary Files

This is a list of supplementary files associated with this preprint. Click to download.

- supportinginformationabdi21404728.docx